THESIS

# EYEWALL REPLACEMENT CYCLE OF HURRICANE MATTHEW (2016) OBSERVED BY DOPPLER RADARS

Submitted by

Ting-Yu Cha

Department of Atmospheric Science

In partial fulfillment of the requirements

For the Degree of Master of Science

Colorado State University

Fort Collins, Colorado

Fall 2018

Master's Committee:

Advisor: Michael M. Bell

Kristen Lani Rasmussen
Steven C. Reising

ABSTRACT

EYEWALL REPLACEMENT CYCLE OF HURRICANE MATTHEW (2016) OBSERVED BY DOPPLER RADARS

An eyewall replacement cycle (ERC) can cause significant changes to the intensity and structure of a tropical cyclone, but the physical mechanisms involved in the ERC process are not fully understood due to a lack of detailed observations. Hurricane Matthew was observed by the NEXRAD KAMX, KMLB, and KJAX polarimetric radars and NOAA P-3 airborne radar when it approached the southeastern United States during an ERC event. The radar observations indicate that Matthew's primary eyewall was replaced with a weaker outer eyewall, but unlike a classic ERC, Matthew did not reintensify after the inner eyewall disappeared.

The evolution of Matthew's ERC is analyzed by examining the observations from the airborne and ground-based radars near the Florida coast. Triple Doppler analysis is performed by combining the NOAA P-3 airborne fore and aft radar scanning with KAMX radar data during the period of secondary eyewall intensification and inner eyewall weakening from 19 UTC 6 October to 00 UTC 7 October. Four passes of the P-3 aircraft show the evolution of the reflectivity, tangential winds and secondary circulation as the outer eyewall became well-established. Further evolution of the ERC is analyzed through reflectivity and tangential wind derived from the single ground-based Doppler radar observations for 35 hours with high temporal resolution every 6 minutes from 19 UTC 6 October to 00 UTC 8 October using the Generalized Velocity Track Display (GVTD) technique. The single-Doppler analyses indicate that the inner eyewall decayed a few hours after the P-3 flight, while the outer eyewall contracted but did not reintensify and the asymmetries increased episodically. The analysis suggests that the resilient outer eyewall was influenced by both environmental vertical wind shear and an internal vortex Rossby wave damping mechanism during the ERC evolution.

# ACKNOWLEDGMENTS

I would like to express my great appreciation to Professor Michael Bell for his mentorship and patience. It is a privilege to have the opportunity to grow along side an extraordinary scientist who has an outstanding knowledge in atmospheric science, strict self-discipline, and is incredibly passionate in conducting research. I would never get through the research difficulties and finish this thesis without his guidance, support and words of encouragement.

I would like to thank my committee members, Professor Kristen Rasmussen and Professor Steven Reising. Their constructive criticism and comments helped finessing my thesis.

I want to show my gratitude to LROSE project team Michael Dixon, Dr. Wen-Chau Lee, and Brenda Javornik in NCAR for their guidance and help. It is my pleasure to work with them.

I am obliged to the Bell research group members for always being supportive with any problem I have with schoolwork and programming, for being fantastic office mates and friends, and for the moral support.

I woud like to thank Alexander DesRosiers for editing P3 radar data together during his REU internship.

Finally, not a single word is enough to describe how much my family and friends mean to me. I am very fortunate to have all the people walking with me along this path.

This research was supported by the National Science Foundation SI2-SSI Award 1661663.

This thesis is typeset in LaTeX using a document class created by Leif Anderson and modified by Christopher Slocum.

TABLE OF CONTENTS

# CHAPTER 1

## Introduction

Hurricane Matthew (2016) was the first Category 5 hurricane in the Atlantic basin since 2007, and caused widespread damage across its destructive path. The most significant impacts were felt in Haiti, with billions dollars of economical loss and over 500 fatalities. In addition, when Matthew moved paralleled to the east coast of Florida, it completed an eyewall replacement cycle (ERC) that was associated with a broadening wind field. The expansion of strong winds impacted the Floridian coastline, and caused structural damage to homes and businesses, along with extensive downed trees and utility lines. The widespread effects made Matthew one of the most destructive hurricane in recent years.

Matthew was observed by three Weather Surveillance Radar 1988 Doppler (WSR-88D) radars in Miami (KAMX), Melbourne (KMLB), and Jacksonville (KJAX) for 35 hours with high temporal resolution every 6 minutes, and National Oceanic and Atmospheric Administration WP-3D (NOAA P-3) airborne radar with high spatial resolution when it approached southeastern United States. The radar observations indicate that Matthew underwent an ERC process where Matthew's primary eyewall was replaced with a weaker outer eyewall, but unlike a classic ERC, Matthew did not re-intensify. The storm was dominated by wavenumber 1 asymmetries with increasing vertical wind shear through the process. The radar loop shows the rotation of non-circular outer eyewalls during the ERC evolution, indicating the internal vortex dynamics also play role in modulating Matthew's asymmetric structure. While the ERC evolution in axisymmetric framework is relatively well-established, the asymmetric internal and external forcing impacting an ERC process has not been well-documented and fully understood.

In order to examine Matthew's asymmetric ERC evolution in detail, a state of the art atmospheric observing system with high temporal and spatial resolution is required. The three ground-based radar continuous observations can acquire Matthew's axisymmetric and asymmetric kinematic structure with high spatial and temporal resolution retrieved by the Generalized Velocity Track Display (GVTD) technique. In addition, since Matthew was observed simultaneously by the P3 tail radar and ground-based radar, it serves as a unique opportunity to compare the wind retrieval fields and examine the validity of Fourier decomposition from airborne pseudo-dual Doppler analysis.

## 1.1 Eyewall Replacement Cycle (ERC)

Hurricane intensity is influenced by a variety of factors such as the surface properties, environmental flow, and internal vortex dynamics. An ERC is known as one of the key processes in modulating TC intensity and structure, and it most frequently happens in intense, highly symmetric systems (Willoughby et al. 1982). The paradigm of a classic ERC in an axisymmetric framework is often associated with three phases: intensification, weakening and reintensification (Willoughby et al. 1982; Black and Willoughby 1992; Sitkowski et al. 2011). The intensification phase starts at the initiation of ERC to near the peak intensity of an inner wind maximum. At this stage, the outer wind maximum is unlikely to be associated with a well-organized convective ring but begins to strengthen. The dynamics of vortex spin-up is proposed by Smith et al. (2009) through two different axisymmetric mechanisms. First, the balanced dynamics above the boundary layer spins up the circulation in response to the diabatic heating generated by convection. Second, unbalanced dynamics due to friction and turbulence within the boundary layer can further intensify the inner core. This study mainly focuses on the first mechanism due to the limitations of the dataset. Although Smith et al. (2009) did not frame the two mechanisms within the context of an ERC, Bell et al. (2012) showed that the secondary eyewall was associated with radial convergence of the angular momentum surfaces as a result of increased diabatic heating in Hurricane Rita (2005), which was consistent the first mechanism.

In the weakening phase, the inner wind maximum decays and the outer wind maximum continues to intensify. Hoose and Colón (1970) first documented a complete concentric ERC during a 34 hour period of radar surveillance in Hurricane Beulah (1967) and suggested that dissipation of the inner eyewall was potentially caused by the downdraft of the secondary circulation of the outer eyewall. The other dynamical reason for the dissipation of the inner eyewall is proposed to result from the hindered inflow by outer eyewall. To understand the intensity changes, the Hurricane Rainband and Intensity Change Experiment (RAINEX) was conducted in 2005, which first documented the eyewall replacement cycle in detail with innovative observation. Observations of Hurricane Rita (2005) indicated that the moat took on the characteristics of a hurricane eye. The relict inner eyewall dissipated in the region where the moat merged with the original eye (Houze et al. 2007). The concentric eyewall evolution in Hurricane Rita was further investigated in Bell et al. (2012). They found that the latent heat produced by the secondary eyewall developed a transverse circulation with subsidence in the moat region. The independent transverse circulation acts as a barrier to the flow which impedes the radial inflow into the inner eyewall and shuts down the energy source. Didlake et al. (2017) provided further evidence that supports the decay of the inner eyewall in large part due to the outer eyewall obstructing the radial inflow when examining the ERC of Hurricane Gonzalo (2014).

When the outer wind maximum surpasses the inner wind maximum, the storm enters the reintensification phase, and the relict inner eyewall weakens and eventually dissipates in the eye. The outer eyewall continues to contract and results in the radial expansion of the maximum tangential wind. The relict inner eyewall circulation modulates the kinematic and thermodynamic structure of a post-ERC eye (Sitkowski et al. 2012). It produces a region of high inertial stability that restricts the transverse circulation in a developing eye. Once the inner eyewall disappears and the inertial stability reduces, the vorticity in the inner core reorganizes, and can cause the vortex to reintensify. The reintensification of the vortex can cause a profound impact on storm surge and wind fetch. An ERC process plays an important role in the oscillation of TC intensity and is still not fully understood due to a lack of detailed observations.

The internal dynamics via axisymmetric and asymmetric mechanisms are proposed to have a profound impact on the hurricane intensification (Reasor et al. 2009). Axisymmetric and asymmetric mechanisms are necessarily coupled together, such as the axisymmetrization of potential vorticity perturbation can lead to intensification of the hurricane (Montgomery and Kallenbach 1997). To accurately predict hurricane intensity, it requires the understanding of both axisymmetric and asymmetric dynamics. Previous studies have investigated individual stages of ERCs mostly in an axisymmetric framework. Although the axisymmetric mechanism can represent part of the TC dynamics, the asymmetries often dominate in a weakening or dissipating TC structure.

## 1.2 Asymmetric TC Dynamics

Numerous studies suggest that asymmetries play an important role in modulation of TC structure and intensity. Asymmetries arise in multiple ways, such as vertical wind shear (Reasor et al. 2000, 2004), vortex Rossby waves (VRWs) (Wang 2002), and convectively-induced mesovortices (vortical hot tower, VHT) (Enagonio and Montgomery 2001). As the asymmetries interact with the parent vortex, they influence storm intensity, structure, and motion. Didlake et al. (2017) found that Hurricane Gonzalo exhibited an azimuthal shift of convective and kinematic asymmetries in ERC evolution, which might result from the interaction with the environmental wind shear. This study focuses on the impact of vertical wind shear and VRWs as represented by the low wavenumber evolution of the derived convective and kinematic variables during the ERC event.

### 1.2.1 Vertical Wind shear

Environmental vertical wind shear (VWS) is regarded as one of the most important environmental predictors of TC intensity changes. VWS often acts as a barrier to TC intensification when under high shear environments (above $11\,\mathrm{m\,s^{-1}}$, Rios-Berrios and Torn (2017)). The vortex's interaction with the evolving environmental flow can influence TC intensity and structure through several pathways: midlevel ventilation (Tang and Emanuel 2012), convective and kinematic asymmetries (Black et al. 2002), and vortex tilt (Jones 1995). Although most studies have discussed VWS as an inhibiting factor to TC intensification, a comprehensive study with a 6-hourly dataset from 1982 to 2014, including best tracks and environmental diagnostics conducted by Rios-Berrios and Torn (2017), shows that moderate VWS ($4.5$ - $11\,\mathrm{m\,s^{-1}}$) associated with other favorable environmental factors (such as high sea surface temperature, sufficient mid-level moisture) can be conducive for TC intensification.

Convective asymmetries are highly dependent on the shear magnitude. Observations of Hurricane Jimena (1991) and Hurricane Olivia (1994) have shown that convection can organize itself into axisymmetric rings and continue to intensify in a weakly sheared environment (Black et al. 2002). However, when a TC encounters high shear, both radar reflectivity and vertical motion possess strong wavenumber 1 components, where the convection and updrafts form in the downshear quadrant of the storm and advect around the eye, which is consistent with the properties of convectively excited vortex Rossby waves. The existence of shear results in the strongest convection on the downshear left (Corbosiero and Molinari 2003). When the cells reach the upshear side of the eyewall, downdrafts dominate below 6 km, associated with evaporative cooling and condensate loading. As the cells propagate toward the right of shear, most hydrometeors have already either frozen or precipitated out. The unloaded cells become weaker and separate from the eyewall. Reasor et al. (2013) composited 75 TC flights and confirmed the azimuthal distribution of the convective and kinematic asymmetry impacted by the vertical wind shear.

Given that VWS tilts the vortex towards the downshear side, vortex realignment is a vital process for a TC to maintain its structure in a sheared environment. Mechanisms have been proposed to explain vortex realignment including vortex precession (Jones 1995) and damping of vortex Rossby waves (VRWs; Reasor et al. (2004)). Jones (1995) has shown that the coupling between upper- and lower-level cyclonic potential vorticity (PV) anomalies results in cyclonic precession of the vortex, and the susceptibility of the vortex to VWS depends on the penetration depth which is a function of increased Coriolis parameter, reduced static stability and increased strength or size of the vortex. Increasing the penetration depth leads to a less tilted vortex. Wang and Holland (1996) found that the simulated TC achieved a quasi-steady tilt in downshear left through the realignment process. Reasor and Eastin (2012) further supported the reduction of vortex tilt in response to the shear forcing using observations of Hurricane Guillermo (1997) during rapid intensification.

#### 1.2.2 Vortex Rossby Wave

The other mechanism of vortex realignment has been observed by Reasor and Montgomery (2001), demonstrating the fundamental role of vortex Rossby waves in the relaxation of a tilted vortex to an aligned state in the presence of shear. VRWs are different from planetary Rossby waves (PRWs). PRWs exist on the meridional gradient of planetary vorticity, but VRWs exist on the radial gradient of storm vorticity. The theory of VRWs serving as an axisymmetrization mechanism of disturbances was first proposed by Montgomery and Kallenbach (1997). The emergence of VRWs has been discussed via the barotropic breakdown of an unstable ring vortex (Schubert et al. 1999) and forced by the environmental shear (Reasor et al. 2004). The VRWs in the inner core propagate radially outward and stagnate at radii of 70-90 km, where the radial vorticity gradient disappears or reverses sign (Wang 2002). The propagation of waves can change the eyewall shape and transport momentum, and they can be seen on radar imagery where the shape of the eyewall is polygonal or elliptical (Kuo et al. 1999).

Kossin and Eastin (2001) used aircraft flight-level data from Hurricane Diana (1994) and Hurricane Olivia (1994) to investigate the kinematic and thermodynamic distributions across the eye and eyewall in the radial profiles from a barotropically unstable state associated with enhanced angular velocity within the eyewall to a stable state associated with nearly monotonic angular velocity. The rapid transition between two regimes suggests the concept proposed by Schubert et al. (1999), in which the enhanced vorticity in the eyewall and decreased vorticity in the eye is associated with barotropic instability, leading to the turbulent exchange between the eye and eyewall via a breakdown of the vorticity ring and polygonal eyewalls, which further results in the rearrangement of the vorticity field. This relaxation process leads to a monotonic vorticity profile within the eye. The reduction of maximum wind can have a substantial impact on the intensity of a mature hurricane. Reasor et al. (2000) also suggested the vorticity redistribution process of Hurricane Olivia (1994) was through propagation of VRWs with airborne dual-Doppler analysis. They found the coupling of spiral convection with wavenumber 2 vorticity bands, which is supported by the numerical study of Wang (2002) with PV budget analysis, indicating the importance of asymmetric transverse circulation in Olivia's inner core. A comprehensive observational study of Hurricane Elena (1985) associated with an elliptical eyewall was examined by Corbosiero et al. (2006), showing the prominent wavenumber 2 components caused by the propagation of VRWs. Rozoff et al. (2008) documented a barotropic experiment where the initial vorticity ring weakens as mesovortex formation makes vorticity generation even less efficient in the maintenance of the vortex. This process can slow down the intensification rate. The above studies support the hypothesis that VRWs play an important role in modulation of hurricane intensity.

### 1.2.3 Interaction between VWS and VRWs

Unlike some studies mentioned above (Schubert et al. 1999; Kossin and Eastin 2001) that suggest VRWs have a negative impact on TC intensity, Reasor and Montgomery (2001) proposed the fundamental role of VRWs in the relaxation of a tilted vortex to an aligned state in the presence of shear leading to vortex realignment. The vorticity of a sheared vortex can be decomposed into the mean state and perturbation state. If the perturbation state interacts with the mean state (the wave-mean flow interaction), it will further result in a resilient vortex, which is called the vortex Rossby wave damping mechanism (Reasor and Montgomery 2001). Reasor et al. (2004) has shown that the VRWs damping mechanism can act to maintain vortex vertical alignment in a sheared environment with a simple linearized PE model that was supported by Hurricane Olivia (1994) analysis. Bell and Montgomery (2008) suggested that mesovortices in Hurricane Isabel (2003) enhanced radial mixing and penetration of low-level inflow with high entropy air into the eye region, resulting in intensifying hurricanes. They hypothesized that VRWs can act as a "turbo boost" to the hurricane heat engine. Hurricane Guillermo (1997) exhibited similar features that suggest vorticity asymmetries in the inner core can yield intensification when a TC is vertically sheared (Reasor et al. 2009).

The above studies have suggested that the interaction between environmental vertical wind shear dynamics and internal vortex dynamics can sustain the vertically sheared vortex, but none of the observations have documented the low wavenumber evolution of kinematic and convective structure in an ERC process due to the lack of observations. As pointed out before, Doppler radars are one of the only tools available to retrieve the three-dimensional structure at high temporal and spatial resolution.

## 1.3 Observations by Doppler radar

Doppler radar has been the most essential tool to observe mesoscale convective and kinematic structure. When a Doppler radar transmits a pulse outward, a single target will shift the frequency of the radar signal depending on its speed in a radial direction. Thus, a Doppler radar can only detect the radial velocity but cannot provide its three-dimensional velocity. To get a full wind field requires the synthesis of wind fields from dual-Doppler observations.

The detailed three-dimensional TC structure is primarily derived from dual-Doppler observations, which is often observed by the tail Doppler radar with fore/aft pointing on the NOAA P3. Aircraft observations have contributed a significant value to the research field. Although dual-Doppler observations can be used to assess snapshots of high resolution kinematic and convective structure, airborne reconnaissance and research missions are rare events in most of the countries impacted by tropical cyclones. In addition, the interactions between physical mechanisms are difficult to be addressed due to the limitations of real-time application and spatial and temporal discontinuities of these observations (Lee et al. 1999). The three-dimensional airflow structure can also be retrieved from dual-Doppler observations when the system is detected by two ground-based radars. Nevertheless, the dual-Doppler radar observations of TC are usually limited by the radar range with only a small portion of the TC (Jou et al. 1996) and extensive radar baselines. The range limitation can restrict the operational exploitation of Doppler measurements. The wind retrieval technique based on single Doppler observations is often required.

Single Doppler radar offers a powerful tool for monitoring TCs close to the coast and landfalling TCs because of the widely distributed of radar network across many countries. A ground-based single Doppler radar can complete each volume scan with high temporal resolution.

Ground-based velocity track display (GBVTD) was developed by Lee et al. (1999), which can retrieve the TC primary circulation from a single Doppler radar. The linear least square methods is utilized to fit Fourier basis functions onto the Doppler velocity, so the along-beam mean wind, axisymmetric radial wind and tangential wind can be retrieved for each radius and altitude based on the Fourier coefficients. The GBVTD-retrieved winds provide a quantitative approach to estimate the primary circulation of TCs from single-Doppler velocity patterns. The tangential and radial velocities in a TC are usually asymmetric, composed of mean flow and waves of all scales. The tangential and radial velocities will appear as a complex waveform that can be decomposed into Fourier components. These Fourier components contain contributions from the individual wavenumbers of the tangential and radial winds at each radius of a TC. The GBVTD technique provides a new way to examine axisymmetric and asymmetric structures of a TC near landfall from single ground-based Doppler radar.

However, the GBVTD technique cannot resolve the asymmetric part of the radial wind and the cross-beam component of mean wind which will alias into the tangential winds and along-beam mean wind. Another limitation is that a ground-based Doppler radar has to be located outside of the radial distance between the radar and the storm center in order to sample the full tangential component of the vortex circulation accurately. In addition, the retrieved asymmetric components of wind field are distorted.

Generalized velocity track display (GVTD) (Jou et al. 2008) is a technique that inherited the roots of GBVTD. It introduces an aspect ratio by multiplying the distance of each gate (D) by measured Doppler velocity ($V_d$) and then scaling by the distance between the radar and the TC center ($R_T$). Key vortex kinematic structures displayed in the $V_d D/R_T$ space simplify the interpretation of the radar signature and eliminate the geometric distortion inherited in the $V_d$ space (Jou et al. 1996). It will be shown that GVTD expands $V_d D/R_T$ into Fourier coefficients in a linear coordinate ($\theta^{'}$) rather than expanding $V_d$ in a nonlinear coordinate ($\psi^{'}$) in GBVTD. The geometry and symbols are displayed in Fig. 2.2. The retrieved wind field from GVTD is no longer limited by the analysis domain due to the required approximation of $\cos\alpha$ in GBVTD (Eq. (5) in Lee et al. (1999)), and the retrieved asymmetric structures are without distortion. Also, the GVTD formulation can be applied to the extensions of the velocity track display (VTD) techniques (e.g. GBVTD-simplex, Lee and Marks (2000)) to improve their performance. Therefore, it not only expands the capability of using ground-based Doppler radar data in TC forecasts but provides researchers an opportunity to examine TC kinematic and some derived dynamic variables (such as vertical velocity, angular momentum, and vertical vorticity).

Beyond all of these advantages, the limitations in the GVTD technique are worth noting. First of all, the retrieved maximum of radial wind ($V_{Rmax}$) from GVTD is more sensitive to the accuracy of the center than the $V_{Rmax}$ derived from the GBVTD technique. Secondly, the mean wind vector is hard to determine when the circulation of the vortex is large. Third, the distance weighting of $V_d D/R_T$ rescales Doppler velocities such that the missing data at a large range may potentially influence the results of GVTD coefficients from least squares fit. Nonetheless, the GVTD technique largely improves and extends the capability of GBVTD, and reduces many of the constraints. Due to these advantages, the GVTD technique is the primary analysis tool in this study. Jou et al. (2008) have tested GBVTD and GVTD technique with idealized Rankine vortices, and confirmed that the GVTD technique is beneficial to retrieve the vortex kinematic structure. However, the accuracy of the asymmetric wind may be degraded, since the retrieved wind neglects all asymmetric radial components.

Besides the concern with the GVTD technique, performing Doppler analysis with the assumption of steady state with aircraft data might not be applicable under all circumstances. In Lee et al. (1994), velocity track display (VTD) technique from a single airborne Doppler radar was utilized to examine Hurricane Gloria (1985) kinematic structure and they compared the results with pseudo-dual Doppler analysis constructed from two orthogonal flight legs with the assumption that the circulation was in a steady state over 1-2 hour period. They concluded that higher wavenumbers tend to be created and the wind maxima was reduced due to the spatial and temporal aliasing in pseudo-dual Doppler analysis. This is another concern for the accuracy of Fourier decomposition with pseudo-dual Doppler analysis.

In this study, we focus on the interaction of Hurricane Matthew with environmental vertical wind shear and internal vortex dynamics of VRWs, documenting the axisymmetric and low-wavenumber evolution in Matthew's ERC event with triple Doppler and single Doppler analyses. The GVTD technique is utilized to diagnose the vortex axisymmetric and asymmetric structure evolution from single Doppler ground-based radar. Past studies have suggested that VRWs are well-coupled with convection (Reasor et al. 2000; Wang 2002; Corbosiero et al. 2006), so the radially outward propagation of inner rainbands could serve as a proxy for VRWs activity. However, the numerical simulation of Hurricane Bill (2009) conducted by Moon and Nolan (2015) suggested that the deformation of spiral inner rainbands from convective clouds resulted from the rapidly rotating TC wind field, rather than the propagation of VRWs since the inner rainbands were not consistently collocated with PV signals. To acquire a better estimation of potential vorticity, our study utilizes tangential winds retrieved by the GVTD technique to examine the VRW activity. In addition, since Matthew was observed by P3 tail radar, concurrently with KAMX ground-based radar, the wind fields retrieved by single Doppler and triple Doppler analyses are compared.

The datasets and analysis methodology are presented in Chapter 2, with the detailed GVTD-improved technique. The results of triple Doppler and single Doppler analyses in axisymmetric framework, and the asymmetric evolution derived from the single Doppler analysis are illustrated in Chapter 3. The comparison between triple Doppler and single Doppler observations will be detailed in Chapter 4. A summary of our results and conclusions are presented in Chapter 5.

# CHAPTER 2

## Data & Methods

The following sections detail the procedure of processing ground-based radar, airborne radar data, the GVTD technique derivation, best track, SHIPS, OISST, and SFMR datasets separately.

### 2.1 Single Doppler Ground-based Radar Data

When Matthew approached the east coast of Florida, continuous radar scans from KAMX, KMLB, and KJAX observed the ERC. The observation period of each radar is listed in Table 2.1, and the location of each radar is displayed in Fig.2.1a. The datasets were obtained from NOAA Archive Information Request System webpage. The radar sweep files were initially processed using an automated quality control (QC) using National Center for Atmospheric Research (NCAR) SoloII software and then manually edited the data to unfold the Doppler velocity aliasing and remove the discontinuities and noise echoes. The edited sweep files applied Radx2Grid, part of the Lidar Radar Open Software Environment (LROSE), for coordinate transformation and interpolation of the fields from plan position indicators (PPIs) (elevation angle, Y, Z) to constant-altitude plan position indicators (CAPPIs) in Cartesian coordinate (X, Y, Z). The gridded domain is 400 km × 400 km with a horizontal grid spacing of 1 km and vertical grid spacing of 0.5 km. The gridded data was further analyzed by the Vortex Objective Radar Tracking and Circulation (VORTRAC) software and to retrieve the kinematic structure by the GVTD technique (Jou et al. 2008).

### 2.2 GVTD technique improvement

The GVTD technique is able to retrieve the axisymmetric and asymmetric components of tangential wind as described previously. The Doppler velocity in Jou et al. (2008) is decomposed into tangential, radial, and mean wind components where storm motion is an implicit element in the mean wind

TABLE 2.1. Details of each ground-based radar observation period and triple Doppler analysis of each aircraft mission with corresponding KAMX observation for this study.

| Radar analysis | Date | Duration |
|---|---|---|
| KAMX | 6-7 Oct 2016 | 1907-0550 UTC |
| KMLB | 7 Oct 2016 | 0125-1800 UTC |
| KJAX | 7-8 Oct 2016 | 1307-0009 UTC |
| Pass 1 | 6 Oct 2016 | 1855-1940 UTC (P3) and 1920 UTC (KAMX) |
| Pass 2 | 6 Oct 2016 | 2020-2105 UTC (P3) and 2040 UTC (KAMX) |
| Pass 3 | 6 Oct 2016 | 2145-2230 UTC (P3) and 2217 UTC (KAMX) |
| Pass 4 | 6 Oct 2016 | 2305-2340 UTC (P3) and 2320 UTC (KAMX) |

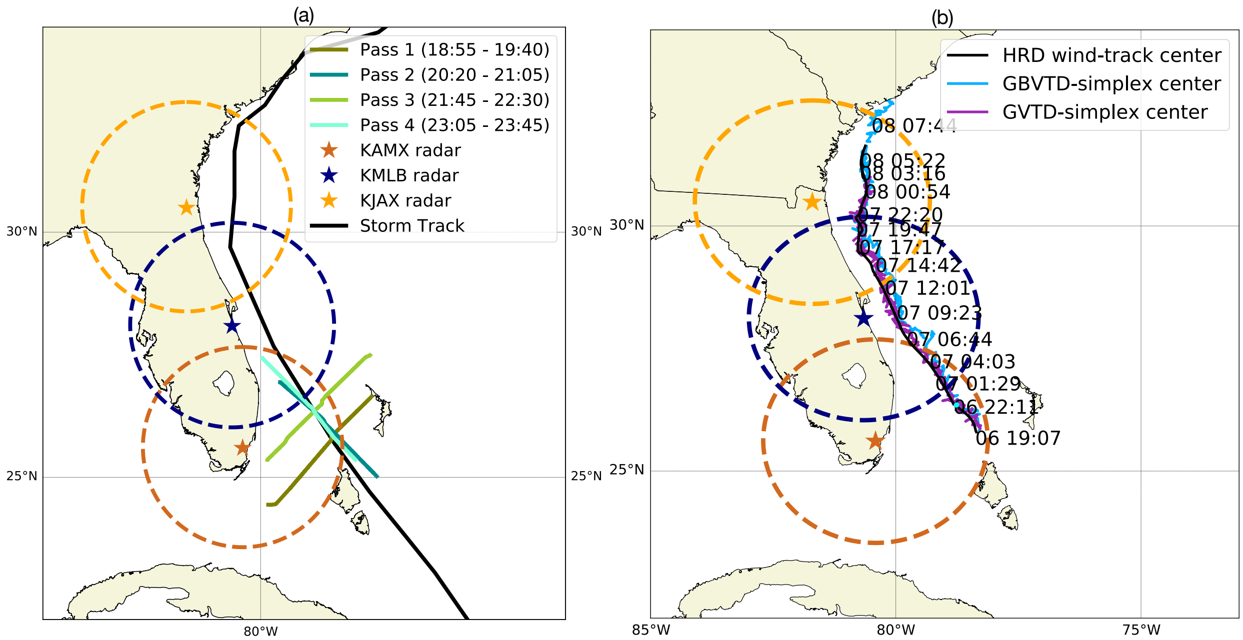


FIG. 2.1. (a) Hurricane Matthew's storm track from best track data (black line) and the deployed observation instruments. Pass 1-4 denote the passage of P-3 plane across the cyclone on 6 October. Colored circles and stars represent the ground-based radar detecting range (230 km) and location of single Doppler radar respectively. (b) Comparison of Hurricane Matthew's track between HRD dynamic center (black line), GBVTD-simplex center (light blue line), and GVTD-simplex center (purple line). Colored circles and stars are the same as (a).

component. Although the environmental wind is an important factor to determine storm motion, the storm motion and environmental wind are not the same component. The divergence of the environmental flow may not be zero since the environmental flow is not constant in the horizontal direction, while the storm motion has no divergence associated with it since it is constant in the horizontal direction (Chan and Gray 1982; Chan 1984). The mean wind ($V_M$) is the average of the environmental flow in the horizontal direction, and changes with each altitude, which is the cause of vertical wind shear. Storm motion ($U_S$, $V_S$) is defined here as the deep layer flow over the whole vortex and does not vary with height or radius. The rest of the terms, such as tangential ($V_T$)and radial ($V_R$) winds, are functions of radius, height and azimuth.

Although the storm motion and mean wind component are combined together in GVTD, they do not have an influence on retrieving the phase and magnitude of asymmetric components of tangential wind. The storm motion and mean wind play a role in the retrieval of the components of mean wind, wavenumber 0 tangential and radial winds. A large error in the retrievals occurs when the storm moves fast or there is a high deviation of direction between mean wind and storm motion. To resolve this error, we rederive the GVTD technique and separate the storm motion from the mean wind component.

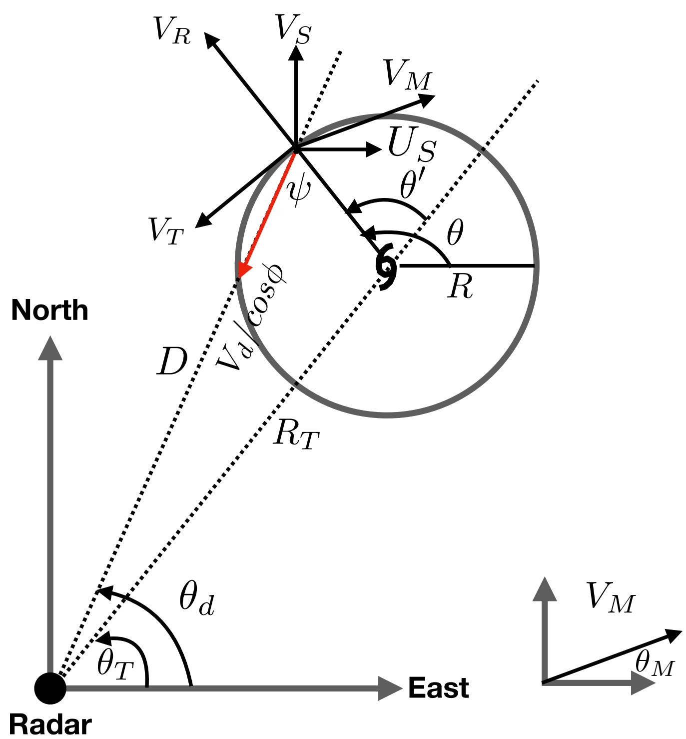


FIG. 2.2. The geometry and symbols used in the formulation of GVTD (modified from Jou et al. (2008)). Red arrow denotes the Doppler velocity.

Following the symbols and geometry utilized in the GBVTD and GVTD technique, the addition of the storm motion to the geometry is illusrated in Fig. 2.2. Starting with the horizontal projection of the Doppler velocity in GVTD (Jou et al. 2008) and GBVTD (Lee et al. 1999)

$$V_d/cos\phi = V_M cos(\theta_d - \theta_M) - V_T sin\psi + V_R cos\psi \tag{2.1}$$

where $\phi$ is the elevation angle of the radar, $\theta_d$ is the mathematical angle of the radar measured from the east, $\theta_M$ is the direction of mean wind, and $\psi$ is the angle composed by the measured radar beam to the radar and the measured radar beam to the storm center. In this study, the storm motion ($U_S$, $V_S$) is added into the equation, and it becomes:

$$V_d/cos\phi = V_M cos(\theta_d - \theta_M) + U_S cos\theta_d + V_S sin\theta_d - V_T sin\psi + V_R cos\psi \tag{2.2}$$

where $\psi = \theta - \theta_d$. Rearranging the Doppler velocity, we obtain

$$
\begin{aligned}
V_d/cos\phi &= V_M cos(\theta_d - \theta_M) - V_T sin(\theta - \theta_d) + V_R cos(\theta - \theta_d) + U_S cos\theta_d + V_S sin\theta_d \\
&= V_M(cos\theta_d cos\theta_M + sin\theta_d sin\theta_M) - V_T(sin\theta cos\theta_d - cos\theta sin\theta_d) \\
&+ V_R(cos\theta cos\theta_d + sin\theta sin\theta_d) + U_S cos\theta_d + V_S sin\theta_d
\end{aligned}
\tag{2.3}
$$

$\theta_d$ can be deduced as:

$$
\begin{aligned}
D cos\theta_d &= R cos\theta + R_T cos\theta \\
D sin\theta_d &= R sin\theta + R_T sin\theta
\end{aligned}
\tag{2.4}
$$

Plugging Eq. 2.4 into Eq. 2.3 and approximating $V_d/cos\phi$ with $V_d$

$$
\begin{aligned}
V_d &= (-V_T sin\theta + V_R cos\theta + V_M cos\theta_M + U_S)(R cos\theta + R_T cos\theta_T)/D \\
&+ (V_T cos\theta + V_R sin\theta + V_M sin\theta_M + V_S)(R sin\theta + R_T sin\theta_T)/D
\end{aligned}
\tag{2.5}
$$

Rearranging Eq. 2.5 and let $\theta' = \theta - \theta_T$, obtaining:

$$
\begin{aligned}
V_d \frac{D}{R_T} &= [V_R \frac{R}{R_T} + V_M cos(\theta_T - \theta_M) + U_S cos\theta_T + V_S sin\theta_T] \\
&- [V_T + \frac{R}{R_T}(V_M sin(\theta_T - \theta_M) + U_S sin\theta_T - V_S cos\theta_T)] sin\theta' \\
&+ [V_R + \frac{R}{R_T} V_M cos(\theta_T - \theta_M) + U_S cos\theta_T + V_S sin\theta_T)] cos\theta'
\end{aligned}
\tag{2.6}
$$

Decomposing $V_d D/R_T$, $V_T$, and $V_R$ into Fourier components in the $\theta'$ coordinates:

$$
V_d \frac{D}{R_T}(R, \theta') = A_0 + \Sigma A_n cosn\theta' + \Sigma B_n sinn\theta' \tag{2.7}
$$

$$
V_T(R, \theta') = V_T C_0 + \Sigma V_T C_n cosn\theta' + \Sigma V_T S_n sinn\theta' \tag{2.8}
$$

$$
V_R(R, \theta') = V_R C_0 + \Sigma V_R C_n cosn\theta' + \Sigma V_R S_n sinn\theta' \tag{2.9}
$$

where $A_n$ ($V_T C_n$ and $V_R C_n$) and $B_n$ ($V_T S_n$ and $V_R S_n$) are the amplitude of the azimuthal wavenumber n cosine and sine components, as defined in Lee et al. (1999); Jou et al. (2008). Substituting Eqs. 2.7, 2.8, and 2.9 into Eq. 2.6, we obtain the following:

$$A_0 = \frac{R}{R_T} V_R C_0 + V_M cos(\theta_T - \theta_M) - \frac{1}{2} V_T S_1 + \frac{1}{2} V_R C_1 + U_S cos\theta_T + V_S sin\theta_T \tag{2.10}$$

$$A_1 = \frac{R}{R_T} V_R C_1 + \frac{R}{R_T}(V_M cos(\theta_T - \theta_M) + U_S cos\theta_T + V_S sin\theta_T) + V_R C_0 - \frac{1}{2} V_T S_2 + \frac{1}{2} V_R C_2 \tag{2.11}$$

$$B_1 = \frac{R}{R_T} V_R S_1 - \frac{R}{R_T}(V_M sin(\theta_T - \theta_M) + U_S sin\theta_T - V_S cos\theta_T) - V_T C_0 + \frac{1}{2} V_T C_2 + \frac{1}{2} V_R S_2 \tag{2.12}$$

$$A_n(n \geq 2) = \frac{R}{R_T} V_R C_n + \frac{1}{2}(V_T S_{n-1} + V_R C_{n-1} - V_T S_{n+1} + V_R C_{n+1}) \tag{2.13}$$

$$B_n(n \geq 2) = \frac{R}{R_T} V_R S_n + \frac{1}{2}(-V_T C_{n-1} + V_R S_{n-1} + V_T C_{n+1} + V_R S_{n+1}) \tag{2.14}$$

The Fourier coefficients can be rearranged to obtain each wave component of the vortex:

$$V_M cos(\theta_T - \theta_M) = A_0 - \frac{R}{R_T} V_R C_0 + \frac{1}{2} V_T S_1 - \frac{1}{2} V_R C_1 - U_S cos\theta_T - V_S sin\theta_T \tag{2.15}$$

$$V_T C_0 = -B_1 - B_3 + \frac{R}{R_T}[-V_M sin(\theta_T - \theta_M) + V_R S_1 + V_R S_3 - U_S sin\theta_T + V_S cos\theta_T] + V_R S_2 \tag{2.16}$$

$$V_R C_0 = \frac{A_0 + A_1 + A_2 + A_3 + A_4}{1 + \frac{R}{R_T}} - V_M sin(\theta_T - \theta_M) - V_R C_1 - V_R C_2 - V_R C_3 - \frac{R}{R_T}(U_S cos\theta_T + V_S sin\theta_T) \tag{2.17}$$

$$V_T S_n = 2A_{n+1} - V_R C_n + V_T S_{n+2} - V_R C_{n+2} - 2\frac{R}{R_T} V_R C_{n+1} \tag{2.18}$$

$$V_T C_n = -2B_{n+1} + V_R S_n + V_T C_{n+2} + V_R S_{n+2} + 2\frac{R}{R_T} V_R S_{n+1} \tag{2.19}$$

Equations 2.15- 2.19 correspond to equations (16)-(20) in Jou et al. (2008) with additional terms of storm motion in Eqs. 2.15- 2.17. The derivation shows that the storm motion is aliased on the components of mean wind, wavenumber 0 tangential and radial wind. The above equations can yield a more accurate estimation with known storm motion. However, this does not solve the problem that the number of unknown variables is greater than the number of equations in Lee et al. (1999) and Jou et al. (2008). We apply the same closure assumptions that the asymmetric component of radial wind is much smaller than the asymmetric component of tangential wind, so the terms associated with radial wind asymmetries can be ignored. Future research is required to obtain a better closure assumption.

#### 2.2.1 Center finding

The GVTD algorithm to retrieve the wind field is highly sensitive to the center location. Jou et al. (2008) had shown that the uncertainty in the center cannot exceed 5 km in order to have a reasonable wind retrieval. There are several ways to identify TC center, such as the geometric center (Griffin et al. 1992), wind center (Wood and Brown 1992), dynamic center (Willoughby and Chelmow 1982) and vorticity center (Marks et al. 1992). The centers identified by different methods are not necessarily collocated, and the range of uncertainties is from a few kilometers or even higher. Since both vorticity centers estimated from the GVTD technique and dynamic centers derived from the aircraft reconnaissance were available, the comparison of the different centers is required in order to have a better result of wind retrieval.

The GBVTD-simplex algorithm is a method to identify tropical cyclone vorticity centers using single-Doppler radar data developed by Lee and Marks (2000). The simplex center is found by maximizing the mean tangential wind within an axisymmetric TC with three operations on a simplex: reflection, contraction, and expansion. The GBVTD-simplex algorithm reduces the uncertainties in estimating TC position and improves the quality of the GBVTD-retrieved TC circulation. The deviation of the true centers to the GBVTD-simplex center in an idealized TC is approximately 340 m. In this study, since the GVTD technique has better wind field estimation, we conducted the GVTD-simplex method to estimate the centers following the GBVTD-simplex algorithm. By maximizing GVTD-retrieved mean tangential wind, using GVTD technique to estimate the TC vorticity center has higher accuracy than the GBVTD technique.

The GVTD-simplex method is performed using the following procedure:

(1) Doppler velocities on a CAPPI were interpolated onto a cylindrical grid with 1-km radial spacing centered at a given TC center.

(2) Find the TC center possessing the highest mean tangential wind within an axisymmetric TC.

(3)Use three operations on a simplex : reflection, contraction, and expansion - to search for a new maximum or minimum in the field around the simplex. We put the dynamic center from Hurricane Research Division as the first guess. The operation process would start from this point and find the circulation center.

To compare the performance of GVTD-simplex and GBVTD-simplex centers, the dynamic centers from Hurricane Research Division (HRD) are treated as the reference center. The continuous centers are interpolated from the dynamic centers with a series of spline curves every two minutes. Figure 2.1b shows that the GVTD-simplex method provides higher accuracy than the GBVTD-simplex method, which is due to the more accurate estimation of axisymmetric tangential wind. Although the GVTD-simplex centers are most likely following the dynamic centers over 35 hours, the accuracy of GVTD-simplex centers are more variable, similar as GBVTD-simplex center (Lee and Marks 2000) and not consistent with different radar (such as KAMX vs. KMLB, and KMLB vs. KJAX). Since the GVTD technique is highly sensitive to the storm center and the dynamic centers are qualitatively and quantitatively better than the simplex centers, our study utilized the dynamic centers to perform the GVTD technique.

### 2.2.2 GVTD analysis

One component of mean flow, axisymmetric (n=0) tangential wind, radial wind, and asymmetric tangential winds (n=1-2) were retrieved by performing a linear least squares fit on $V_d D/R_T$ in a TC centered cylindrical coordinate, where $V_d$ denotes the Doppler velocity, $D$ denotes the radial range between a pulse volume and the radar, and $R_T$ denotes the radial distance between the TC center and the radar. All data within 1-km radius-wide annulus are included in the linear least squares fit. To deal with missing data in observational radar data and reduce the influence of outliers, the truncation of the Fourier series follows Lee et al. (2000) (Table 2.2), which is consistent with the restriction of maximum allowable gap size in Lorsolo and Aksoy (2012)'s work. They have shown that the maximum allowable gap size varies with number of gaps and noise. If more gaps are present in the signal, the maximum allowable gap size is greater than originally suggested in Lee et al. (2000). We allowed the maximum wavenumber up to wavenumber 2 in the retrieved tangential wind in this study. Applying those criteria reduces retrieval errors, and eliminates some outliers. The Fourier decomposition of reflectivity with linear least squares fit algorithm was also applied by the same criteria to retrieve low-wavenumber Fourier components (n=0-2).

TABLE 2.2. The maximum allowable data gap determines the maximum wavenumber used in the least squares fit.

| Wavenumber | Gap($^o$) |
|---|---|
| 0 | $\leq 180$ |
| 1 | $\leq 90$ |
| 2 | $\leq 60$ |

Once the axisymmetric tangential and radial winds are derived at each radius and height, the axisymmetric vertical vorticity as $\bar{\eta} = \bar{V_T}/r + \partial \bar{V_T}/\partial r + f$ is then calculated from the axisymmetric circulation in this study, where$\bar{\eta}$ denotes the axisymmetric vertical vorticity, $\bar{V_T}/r$ denotes the curvature vorticity, $\partial \bar{V_T}/\partial r$ denotes the shear vorticity, and $f$ denotes the Coriolis parameter (assumed constant). The axisymmetric tangential wind dominates other higher order terms due to the larger magnitude of coefficients compared to the other wind components, while the axisymmetric radial wind is more sensitive to the errors of TC center estimation and mean wind component (Lee et al. 2000). Hence, we only discuss the tangential wind in this study.

The GVTD-technique is a primary research tool to examine the vortex kinematic structure, but neglecting the asymmetric radial wind in real cases to close the underdetermined equations remains a issue. The primary motivation of this study is to compare the GVTD-technique with wind-synthesis analysis in a real case, which none of the previous studies have done before. Airborne and ground-based radar collected data simultaneously when Matthew traveled along the east coast of Florida, provides a unique opportunity to evaluate the wind retrievals. The comparison of retrieved kinematic structures between two radars will be detailed in Chapter 4.

## 2.3 Aircraft radar data

The NOAA P-3 (hereafter as P3) aircraft was involved in the reconnaissance mission during 19 UTC 6 October to 00 UTC 7 October. The P3 was equipped with a tail Doppler radar, which alternately changed the pointing direction fore/aft in order to obtain pseudo dual-Doppler measurements. It documented the period of ERC during the intensification and weakening stages. The data was obtained from the NOAA Aircraft Operations Center (AOC) webpage. The flight track of the P3 was across the tropical cyclone center to collect data for four passes. Each pass was 30 - 60 minutes apart. The window of the four passes is listed in Table 2.1, and the location of each pass is shown in Fig. 2.1a. These four passes are analyzed in detail for this study to examine the changes in kinematic and convective structure with high spatial resolution over four hours.

### 2.3.1 Radar data quality control (QC) and reflectivity correction

To ensure data quality, the P3 radar data was first corrected for navigation errors to reduce the velocity bias (Testud et al. 1995). Then, the radar sweep files were quality controlled with the algorithm developed by Bell et al. (2013) utilizing NCAR SoloII software. The "medium" quality control script was applied to the data, which eliminated most of ground clutter and noise data automatically, and then the rest of the non-meteorological noise and clutter were manually edited.

Comparing the reflectivity field from the X-band P3 data to S-band KAMX radar, it was found that there was a low bias. To ensure a more accurate convective structure in the upcoming triple Doppler analysis, it requires the reflectivity field in P3 data to be corrected before performing triple Doppler analysis. The ground-based radar data was treated as a "true" measurement with the assumption that it was well-calibrated. Since the KAMX radar has the limitation on detecting range, correcting the reflectivity field only utilized the reflectivity in the inner core of vortex (approximately 80 km × 80 km) from the altitude of 4.5 km to 8 km where detected by both radars. The reflectivity correction procedure is listed here:

(1) Interpolate both P3 and KAMX reflectivity field onto a Cartesian grid point with the same resolution by Spline Analysis at Mesoscale Utilizing Radar and Aircraft Instrumentation (SAMURAI) software. We will introduce the SAMURAI software in the following section.

(2) Subtract the reflectivity field from KAMX with P3 data. The bias between two radars resulted in a Gaussian distribution with the maximum centered at -8 dBZ, suggesting that the P3 has a lower bias than KAMX (Fig. 2.3).

(3) Convert the biased dBZ into linear reflectivity factor (Z) space, and take the median of biased reflectivity factor. The dBZ offset value of P3 is -8.375 dBZ.

(4) Add 8.375 dBZ back to the whole domain of P3 original data.

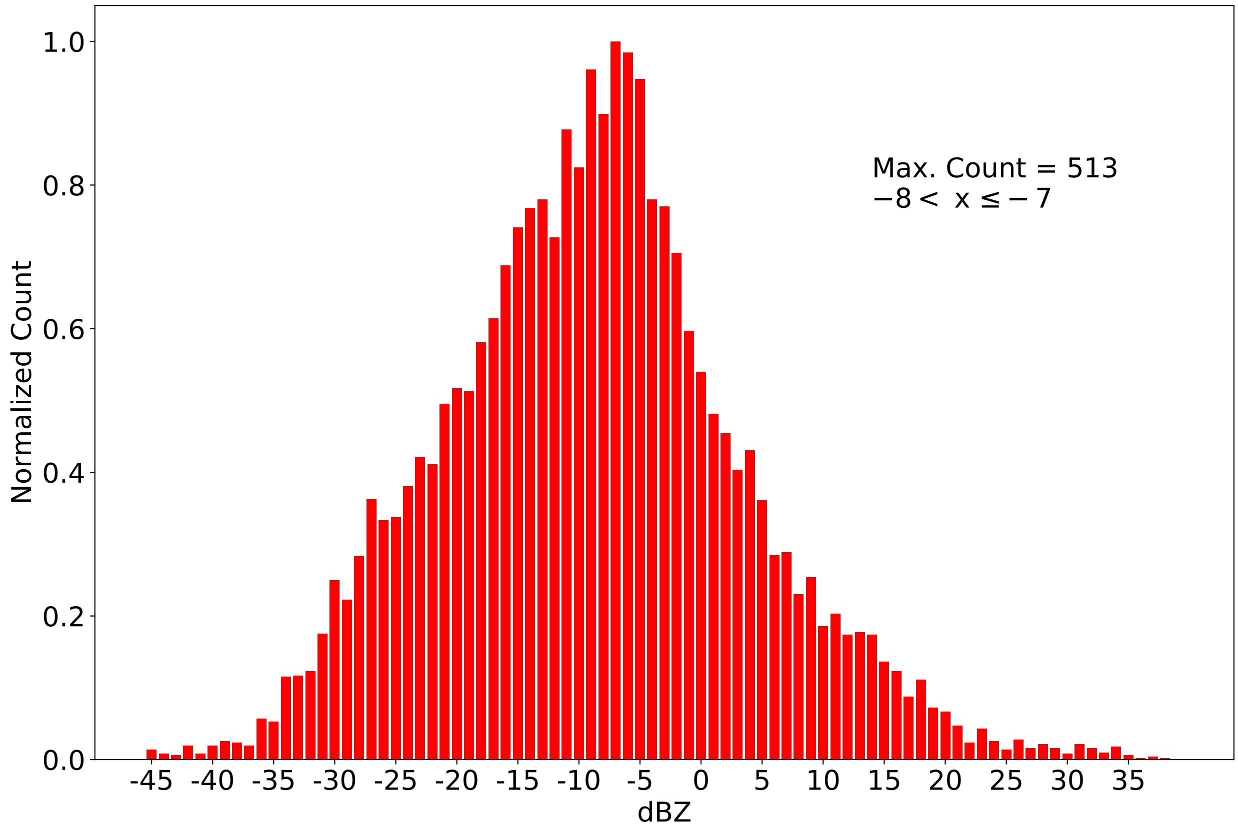


FIG. 2.3. Normalized distribution of reflectivity difference (dBZ) between the P3 tail radar reflectivity field and the KAMX radar reflectivity field.

Figure 2.4 displays the reflectivity field in the inner core of the storm at the altitude of 5.5 km from the KAMX radar data, and P3 data before/after reflectivity correction. It shows that the corrected reflectivity in P3 data is more comparable to the reflectivity field from the KAMX than the uncorrected one. Hence, the triple Doppler analysis can be performed from the bias-corrected P3 data and KAMX data.

### 2.3.2 Triple Doppler analysis

KAMX and P3 simultaneously collected the data from Hurricane Matthew when it approached Florida. KAMX radar has larger data coverage, but P3 has higher spatial resolution due to its closer range. Doppler data from multiple platforms can provide better spatial coverage and geometry, and this combined analysis is referred to as "triple-Doppler" analysis. After conducting the reflectivity correction on the P3 data, each pass and one volume of KAMX data were synthesized at 1-km horizontal grid spacing and 0.5 km vertical grid spacing with SAMURAI (Bell et al. 2012). SAMURAI is a 3D variational data assimilation tool that uses cubic b-splines to find the most likely state of the atmosphere given a set of observations. The storm center and storm motion were both estimated using the dynamic

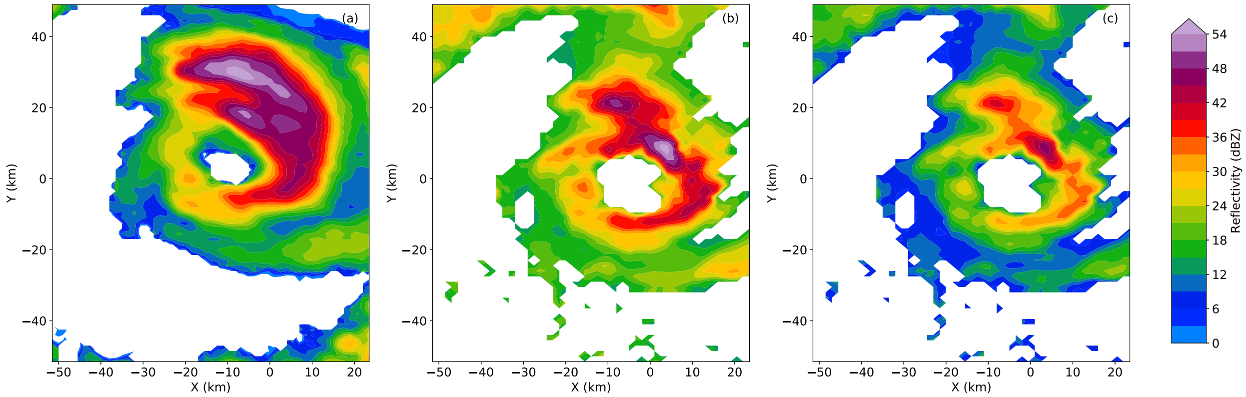


FIG. 2.4. Reflectivity correction comparison. (a) Reflectivity field from KAMX radar at 1920 UTC 6 October, (b) corrected reflectivity from P3 radar, and (c) uncorrected reflectivity from P3 radar pass 1 analysis at the altitude of 5.5 km.

center (Willoughby and Chelmow 1982). The analysis track for the triple Doppler analysis was linearly interpolated from each dynamic center with the given storm motion. The analysis was initially performed on a Cartesian coordinate and then interpolated onto a cylindrical coordinate with azimuthal resolution of 1 degree and radial resolution of 1 km.

The local wind shear magnitude and direction were derived from the triple Doppler analysis, following the procedure proposed by Marks et al. (1992). The storm-relative horizontal wind field ($V_r$)in a cylindrical coordinate system centered on the storm can be decomposed into:

$$V_r(r,\theta,z) = \bar{V_r}(z) + V'(r,\theta,z) \tag{2.20}$$

where r is radius, $\theta$ is azimuth, z is height, $\bar{V_r}(z)$ is the horizontally averaged wind vector over the radius and azimuth, and $V'(r,\theta,z)$ is the deviation from $\bar{V_r}(z)$. $\bar{V_r}(z)$ can be expressed as:

$$\bar{V_r}(z) = \frac{1}{2\pi}\int_0^{2\pi}\int_0^{r_{max}} V_r(r,\theta,z)\,dr\,d\theta \tag{2.21}$$

If the horizontal wind field is from a circular symmetric vortex with no steering flow, $\bar{V_r}(z)$ would be zero. Nevertheless, if the vortex is embedded in the steering flow, the averaged horizontal wind field would equal to the mean wind component. Thus, the local wind shear can be approximated by subtraction of the mean wind component from the altitude of 12 km to 1.5 km. In our study, we calculated

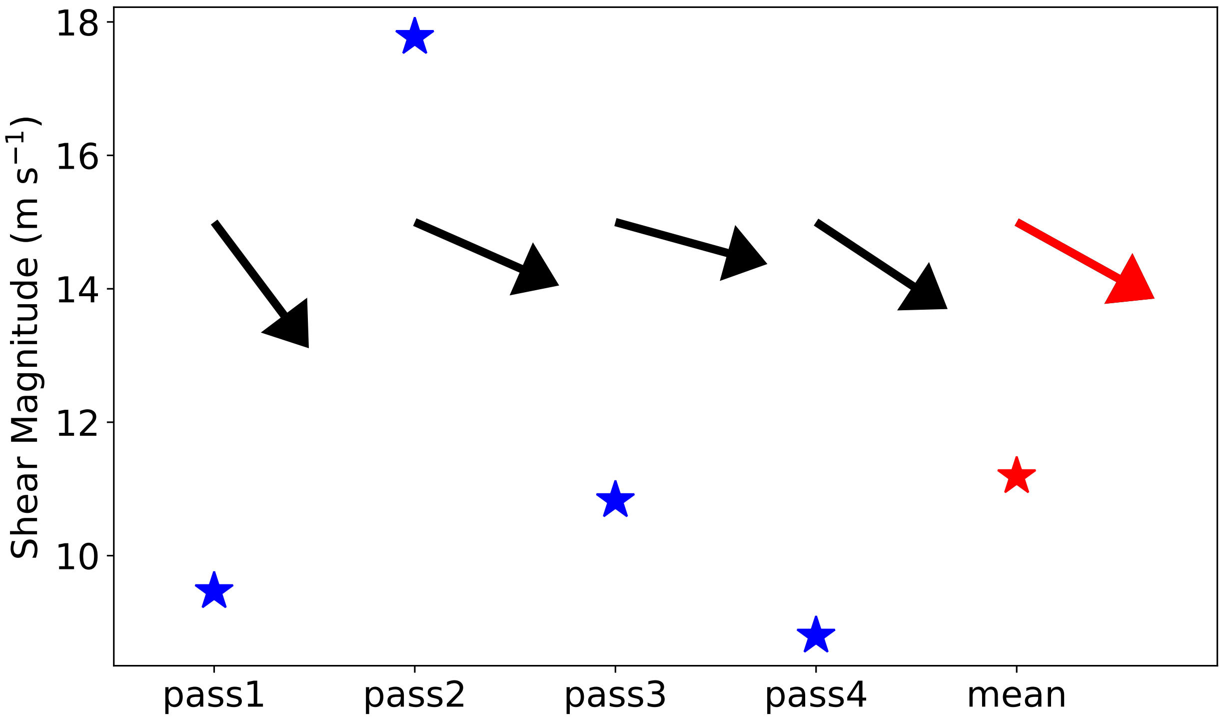


FIG. 2.5. The local wind shear of each pass. Black arrow denotes the direction, and the blue star denotes the shear magnitude. Red arrow and star denote the average of four passes.

the mean wind component averaged from the vortex inner core area within the radius of 60 km. Figure 2.5 displays the estimation of local shear from the four passes. The shear direction and magnitude from four passes are mostly similar except for pass 2 associated with estimated higher shear. Thus, we calculated the local shear averaged over four passes to represent the effective shear. The main purpose for estimating the local wind shear is that the vortex possibly modified the local environment near the inner core of the vortex and affected the environmental shear.

### 2.4 Best track, SHIPS and OISST

The intensity and analysis track details for Hurricane Matthew are obtained from the National Hurricane Center (NHC), while the environmental vertical shear through Matthew's lifetime is from the Statistical Hurricane Intensity Prediction Scheme dataset (SHIPS; DeMaria et al. (2005)). The environmental vertical wind shear variables diagnose in this study is 850-200 hPa shear with vortex removed and averaged from 0-500 km relative to 850 hPa vortex center. The daily sea surface temperature (SST) on 7 October is obtained from the Daily Optimum Interpolation Sea Surface Temperature dataset from the NOAA National Centers for Environmental Information (NCEI; www.ncdc.noaa.gov/oisst).

## 2.5 SFMR dataset and satellite microwave imagery

The measurements of surface wind during the four passes are obtained from the Stepped Frequency Microwave Radiometer (SFMR; Uhlhorn et al. (2007)). The SFMR was flown on the P3 aircraft, and estimated surface brightness temperature at six C-band channels. The estimation of surface wind speed is derived from a geophysical model function (GMF) relating surface emissivity and wind speed. The satellite microwave images are acquired from the Naval Research Laboratory Monterey Tropical Cyclones website (www.nrlmry.navy.mil/TC.html). The satellite images are of the 89-, 91-GHz channel from F-16, F-17, F-18 and GCOM-W1 satellites. The cold (red) brightness temperature in these two channels are primarily influenced by ice-phase hydrometeors which are often associated with deep convection. Thus, the two channels are able to identify the distribution of deep convection in the storm, providing an observation platform to study an ERC event.

# CHAPTER 3

# Results

## 3.1 Hurricane Matthew (2016)

The NHC best track and intensity are shown in Figs. 3.1 and 3.2 for Hurricane Matthew. Hurricane Matthew originated from an African easterly wave and became a tropical storm on 28 September. Matthew underwent a 24-hour period of rapid intensification (RI) between 00 UTC 30 September and 00 UTC 1 October when it passed over the warm Caribbean water and reached Category 5 intensity on 1 October at 13.4 ° latitude, with minimum pressure of 942 hPa and maximum sustained surface winds of 145 knots. Matthew set a new record as the southernmost hurricane to reach Category 5 intensity at the lowest latitude in the Atlantic Basin. The intensity of Matthew then began to weaken while moving northward under a moderate shear environment. As Matthew made landfall in Haiti and interacted with the mountainous region, its low-level circulation was disrupted and the intensity decreased to Category 3. After the next 18 hours, Matthew reintensified by 12 UTC 6 October, and reached Category 4 intensity. The storm then traveled along the east coast of the United States from 6 October through 9 October, it completed an ERC, and then made a right turn to the eastern Atlantic, where it dissipated. Figure 3.1 shows that Matthew moved over a relatively colder ocean surface on 7 October, indicating that the environment was less favorable for reintensification. Figure 3.2 denotes our analysis period during the weakening and reintensification stages of Matthew. The overlap between triple Doppler and single Doppler radar analyses is from 19 UTC 6 October to 00 UTC 7 October.

The 89-GHz and 91-GHz microwave satellite imagery displays the ERC evolution of Matthew (Fig. 3.3). At 2319 UTC 5 October (Fig. 3.3a), deep convection started to form outside the primary eyewall and a spiraling banding structure became evident by 1150 UTC 6 October (Fig. 3.3b), indicating the development of a secondary eyewall. The signature of a concentric eyewall where the inner eyewall was bounded by a nearly circular band of precipitation was observed at 1656 UTC 6 October (Fig. 3.3c). Figure 3.3d shows that the convection in the inner eyewall had weakened and by 1221 UTC 7 October, the inner eyewall almost disappeared and was replaced by the secondary eyewall (Fig. 3.3e). After the absence of the inner eyewall, Matthew became asymmetric and the convection was concentrated on the north side of storm (Fig. 3.3f), suggesting that vertical wind shear played an important role at this time.

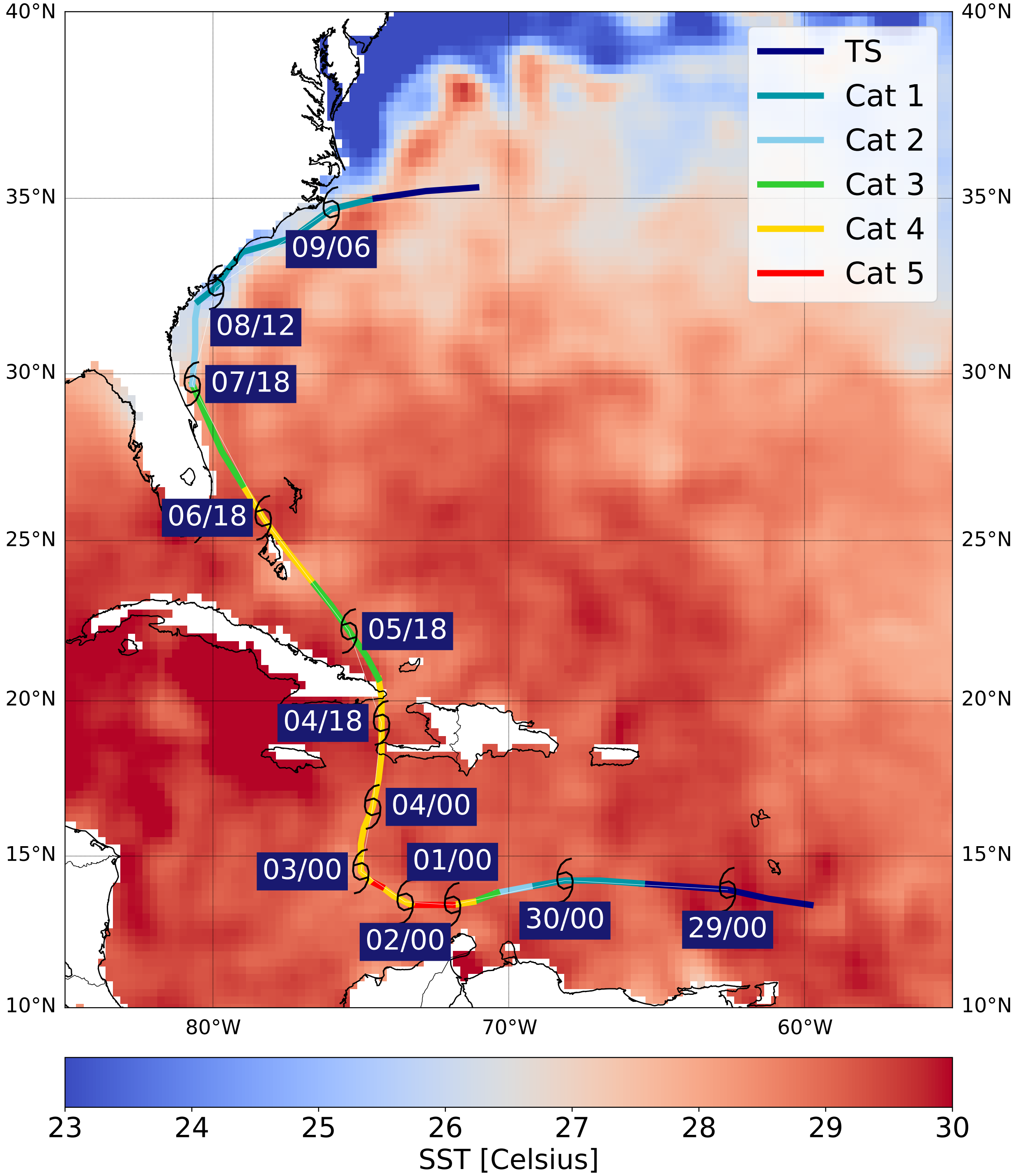


FIG. 3.1. Best track of Hurricane Matthew from the National Hurricane Center (NHC) with dates/UTC in September and October 2016. The shading denotes the SST of 7 Oct 2016.

The vertical wind shear evolution throughout Matthew's life cycle is depicted in Fig. 3.4. The shear magnitude was low to moderate with westerly shear through the earlier period. When Matthew initiated the ERC, it was accompanied by increasing vertical wind shear that was mainly southwesterly and

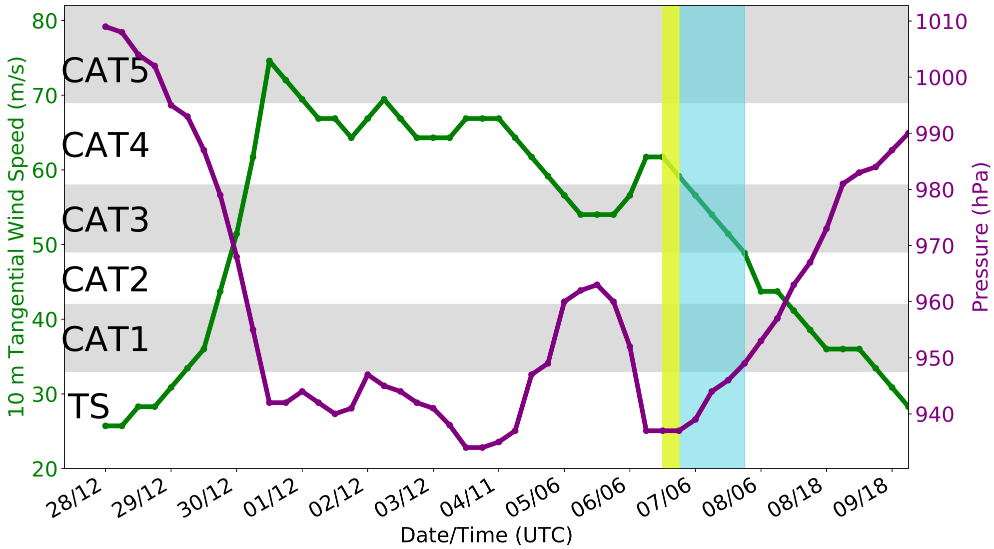


FIG. 3.2. Central pressure and maximum wind speed throughout the lifetime of Matthew. Yellow line represents the analysis period of the triple Doppler analysis from 19 UTC 6 to 00 UCT 7 October. Light blue shading marks the analysis period of the single Doppler analysis from 19 UTC 6 to 00 UCT 8 October.

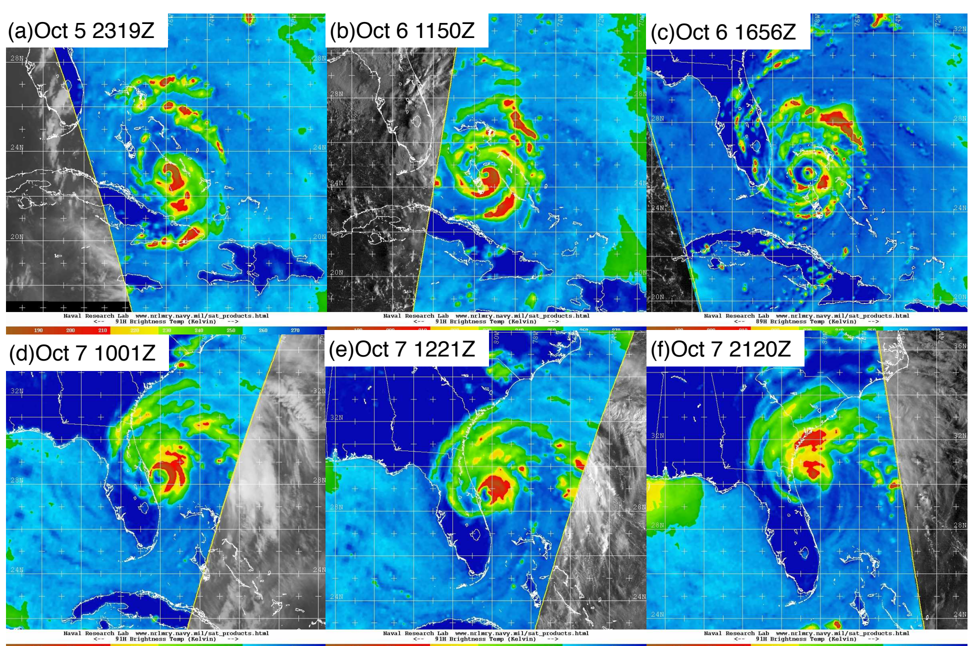


FIG. 3.3. (a) Microwave imagery of brightness temperatures taken at (a) 2319 UTC 5 Oct., (b) 1150 UTC 6 Oct., (c) 1656 UTC 6 Oct., (d)1001 UTC 7 Oct., (e) 1221 UTC 7 Oct., and (f) 2120 UTC 7 Oct., showing the ERC evolution of Hurricane Matthew. Images are from from the Naval Research Laboratory Monterey Tropical Cyclones webpage.

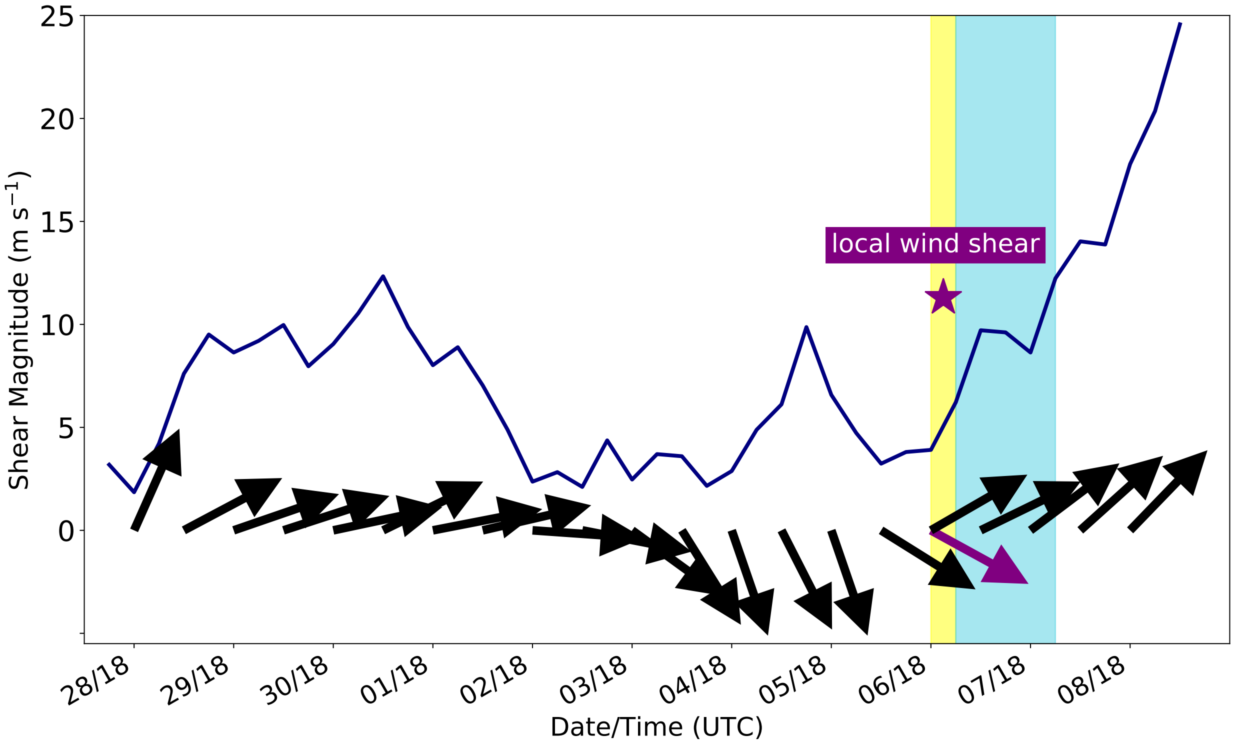


FIG. 3.4. Black arrow indicates the direction of vertical wind shear and blue line is the shear magnitude of the 850-200 hPa environmental shear averaged from 0-500 km distance from the center of 850 hPa vortex (SHDC and SDDC). They are derived from the Statistical Hurricane Intensity and Prediction Scheme (SHIPS) dataset. Westerly shear is associated with a 90 ° heading. The purple arrow and star represent the local shear direction and magnitude calculated from triple Doppler analysis which averaged from 0-60 km distance from the dynamic center from Hurricane Research Division (HRD). The light yellow shading denotes the analysis period of the triple Doppler analysis, and the light blue shading denotes the analysis period of the single Doppler analysis.

strengthened rapidly near the end of observation, which was associated with the increasing asymmetry of Matthew. The northwesterly local wind shear was much higher than the southwesterly environmental wind shear, suggesting that the vortex modified the local environment.

Figure 3.5 denotes the surface wind of the SFMR analysis using 1-2-1 filter to smooth the data from pass 1 through pass 4. The P3 track corresponds to Fig. 2.1a. It shows that a secondary wind maximum on one side of the storm was detected by SFMR on pass 1 of approximately 30 m s$^{-1}$ and the wind field became more symmetric on pass 2. The maximum wind in the inner eyewall then weakened from 52 m s$^{-1}$ to 45 m s$^{-1}$ within five hours. On the other hand, there was a intensifying trend of the secondary wind maximum. The surface wind evolution confirmed the inner eyewall weakened while the outer eyewall strengthened. In addition, a broadening of the wind field was observed, suggesting an undergoing ERC process.

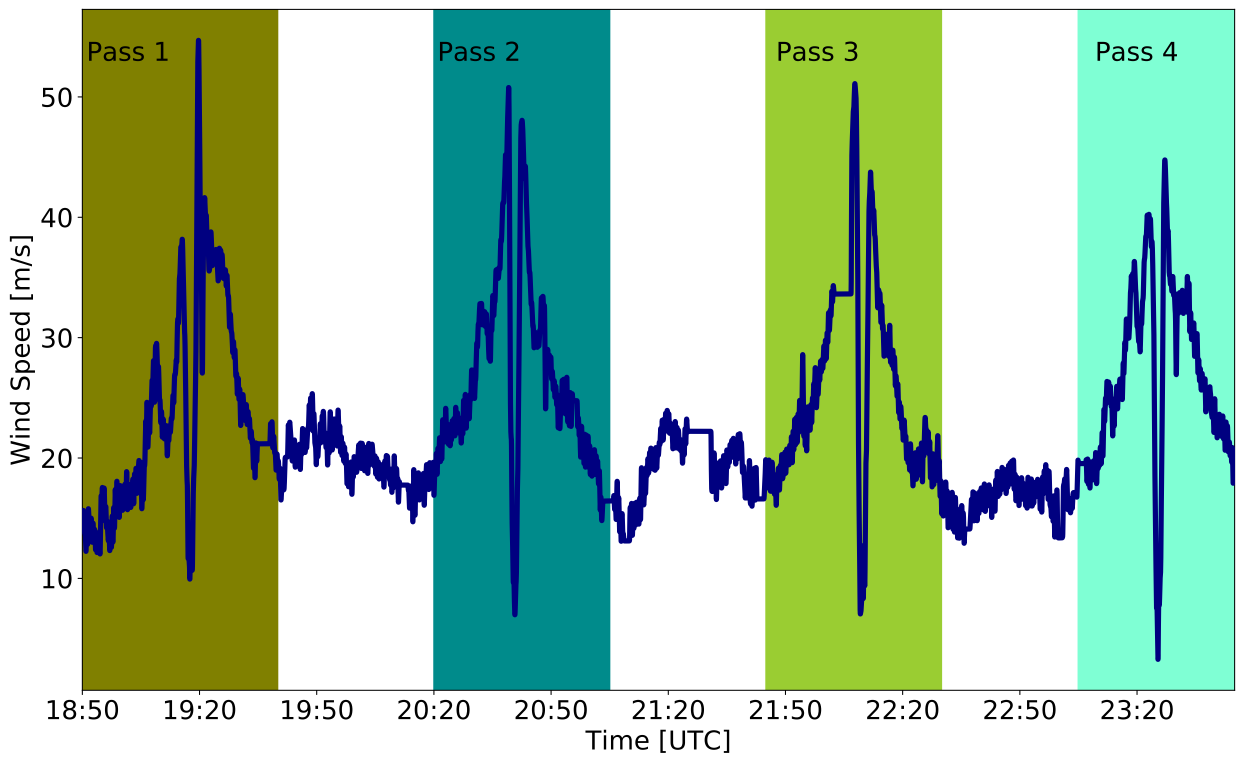


FIG. 3.5. The surface wind evolution from pass 1 through pass 4 ($6^{th}$/19Z-$7^{th}$/00Z). Olive shading is for pass 1, dark cyan shading is for pass 2, yellow green is for pass 3, and aquamarine is for pass 4.

## 3.2 Axisymmetric Structure and Evolution

### 3.2.1 Triple Doppler analysis

Four passes of triple Doppler analysis corresponds to the start of the weakening stage of the inner eyewall and developing stage of the outer eyewall. Figure 3.6 shows the azimuthally-averaged convective and kinematic structure and evolution. During the four passes, the inner eyewall was associated with a nearly circular convective ring with maximum reflectivity located in the down-shear quadrant (See Fig. 3.9a), consistent with previous studies (Corbosiero and Molinari 2002). Pass 1 (Fig. 3.6a) shows that the inner eyewall had its greatest vertical velocity at 11 to 13 km altitude, where the flow turned into radial outflow associated with an overturning circulation. The primary circulation (tangential wind) of the inner eyewall embedded in the reflectivity tower had a peak value of 50 m s$^{-1}$, extending vertically to 4 km. The moat was delineated by a sharp radial gradient of reflectivity (between 35 - 45 km radius), where the region with low reflectivity between the two eyewalls was collocated with downward motion. The downdraft was strongest at upper levels (approximately $-2$ m s$^{-1}$) and extended to low levels (2 km). In the outer eyewall region (between 50 - 75 km radius), the convection was broad

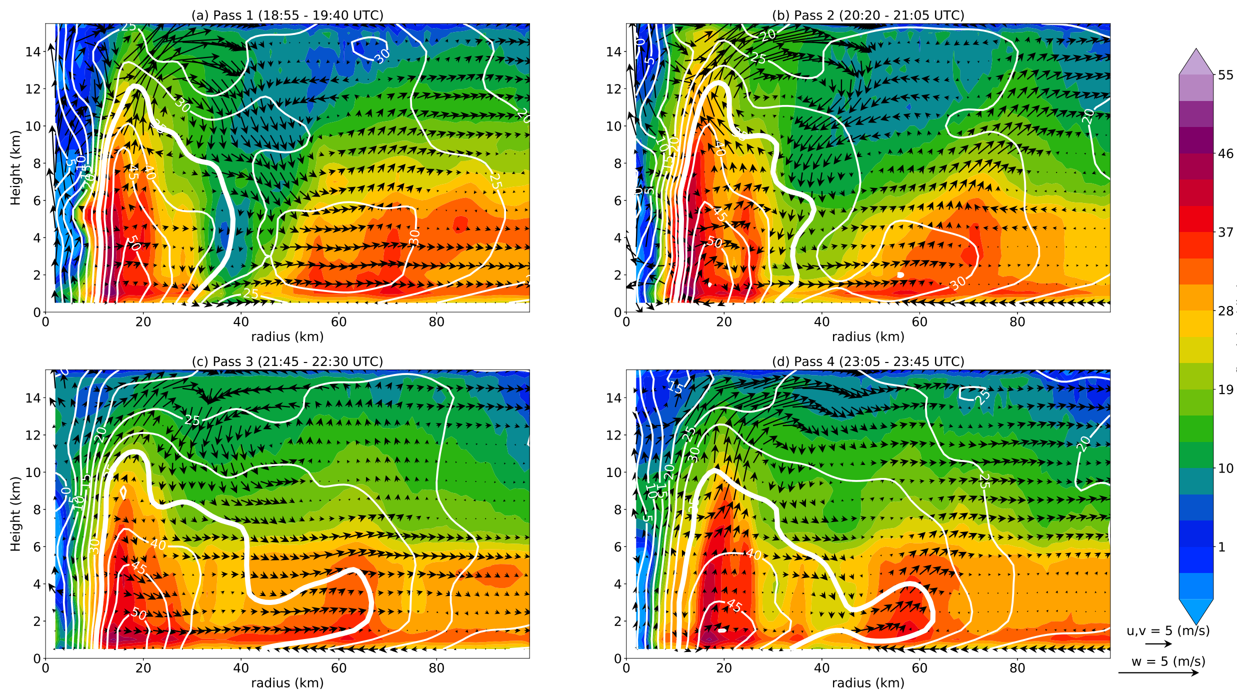


FIG. 3.6. Azimuthally-averaged reflectivity (shaded), primary circulation (white contour, m s$^{-1}$) and secondary circulation (vector) derived from P-3 tail radars. Thick white contour highlights azimuthally-averaged tangential wind of 35 m s$^{-1}$. (a) Pass 1 (18:55 - 19:40 UTC) (b) Pass 2 (20:20 - 21:05 UTC) (c) Pass 3 (21:45 - 22:30 UTC) (d) Pass 4 (23:05 - 23:45 UTC)

and shallow, suggesting that the outer eyewall was still dominated by the rainband features. Although the developing outer eyewall was impacted by the inner eyewall outflow, a tangential wind maximum (30 m s$^{-1}$) in the outer eyewall region was observed, and is associated with a growing updraft in the mid to upper levels. The secondary circulation of the secondary eyewall was vertically shallower compared to the primary eyewall, which is consistent with Hence and Houze (2012).

The inner eyewall reached its peak intensity on pass 2 (Fig. 3.6b), where the primary circulation intensified and the updraft was more vigorous. The moat was starting to fill with some stratiform precipitation, suggesting the descending flow outside of the inner eyewall decreased. The maximum vertical velocity increased at mid-levels (3-8 km), which was fed with increasing low-level radial inflow, consistent with Didlake and Houze (2011). At pass 3 and 4 (Fig. 3.6c and d), the inner eyewall started to weaken, accompanied by the decaying radial gradient of tangential wind and secondary circulation. The moat signature disappeared, filling in with stratiform precipitation. The development of the outer eyewall appeared to follow the expanding tangential wind field, which is highlighted by the thick white contour of 35 m s$^{-1}$ tangential wind, and the formation of an independent secondary circulation. The

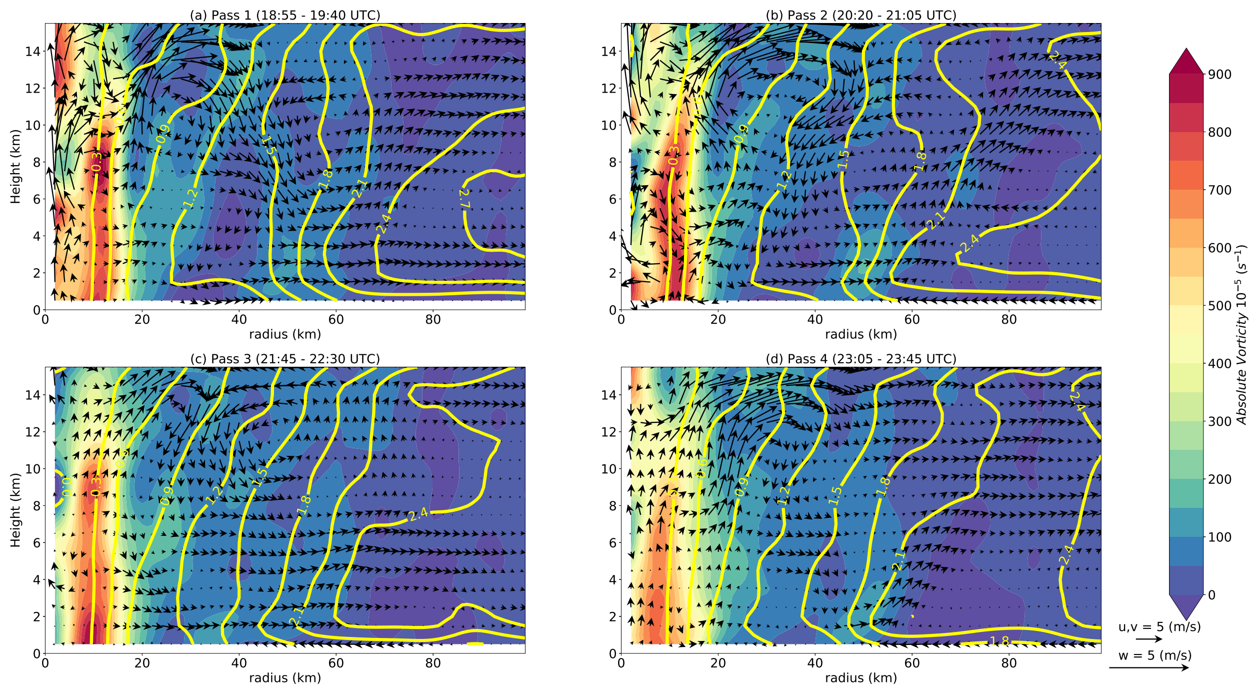


FIG. 3.7. Azimuthally-averaged absolute vorticity (shaded, $10^{-5}$ s$^{-1}$), absolute angular momentum (yellow contour, $10^{6}$ m$^{2}$ s$^{-1}$) and secondary circulation (vector) derived from P-3 tail radars. (a) Pass 1 (18:55 - 19:40 UTC) (b) Pass 2 (20:20 - 21:05 UTC) (c) Pass 3 (21:45 - 22:30 UTC) (d) Pass 4 (23:05 - 23:45 UTC)

outer eyewall became more consolidated on pass 4, associated with increasing upward motion from the low to mid levels and low-level radial inflow layer.

Figure 3.7 shows the azimuthally-averaged absolute vorticity, angular momentum, and kinematic structure evolution. The absolute vorticity field in pass 1 (Fig. 3.7a) shows that the vorticity tower was upright and located along the inner edge of the inner eyewall (Fig. 3.6a, reflectivity), suggesting the effect of frictional convergence and vortex stretching (Bell and Montgomery 2008; Didlake and Houze 2011). The moat region was associated with weak vorticity and bounded by two eyewalls with enhanced vorticity. The secondary circulation followed the angular momentum surfaces in general, suggesting that the angular momentum was approximately conserved above the boundary layer. The maximum vorticity in the outer eyewall region was elevated (between 40 - 60 km radius), but the value was much weaker compared to the vorticity in the inner eyewall (exceeded $8 \times 10^{-3}$ s$^{-1}$).

As the inner eyewall decayed and the tangential wind field expanded, the radial gradient of vorticity decreased through passes 1 - 4 (Fig. 3.7a - d). This evolution suggests that the horizontal mixing of the vorticity between the eye and moat increased, causing decreased vorticity in the inner eyewall and increased vorticity in the moat, consistent with the theoretical work of Schubert et al. (1999); Kossin and

Eastin (2001) and observational studies of Bell et al. (2012). The enhanced vorticity in the outer eyewall region extended to the lower levels and became concentrated at pass 4. The radial convergence of angular momentum surfaces in the outer eyewall region was collocated with the enhanced vorticity, and the surfaces ($1.2$ - $2.1 \times 10^6$ m$^2$ s$^{-1}$) moved radially inward over the analysis period, which was related to the expansion of the tangential wind field (Fig. 3.6d). The above features suggest an undergoing ERC process.

To investigate details on the dynamical interaction between the inner and outer eyewalls, Figure 3.8 shows the azimuthally-averaged divergence and radial flow structure and evolution. The inner eyewall on pass 1 can be identified by a convergence zone extending to 12 km altitude. However, the convergence zone started to bend outward (Fig. 3.8b - d), and the inner eyewall was coupled with weak convergence at low-levels and divergence at mid-levels in pass 4, indicating increasing divergence of the reflectivity tower aloft and subsequent weakening of the inner eyewall. When the outer eyewall was developing, the low-level inflow became stronger and deeper, where the convergence was reinforced at the leading edge of the strong inflow and lifted up the moist air (between 40 - 100 km radius, Fig. 3.8c and d), suggesting that the decaying inner eyewall was in response to lack of inflow due to the strong radial convergence at the outer eyewall. This mechanism is known as the barrier effect which impedes the radial inflow into the inner eyewall and shuts down the energy source, and has been discussed in previous observations of ERC evolution in Hurricane Rita (2005) (Bell et al. 2012) and Hurricane Gonzalo (2014) (Didlake et al. 2017).

The moat signature (between 20 - 40 km radius) was originally associated with low-level divergence (0 - 2 km altitude) and mid-level convergence (2 - 6 km altitude, Fig. 3.8a). As the secondary circulation of the inner eyewall decayed, the outflow of the inner eyewall weakened and the moat region dissapated, which was associated with decaying of convergence aloft and low-level divergence, consistent with the reflectivity evolution (Fig. 3.6). The convergence started to increase in the low-level between the radius of 40 to 60 km on pass 1, and intensified through passes, relating to a stronger inflow layer. The intensification is consistent with the first axisymmetric intensification mechanism proposed by Smith et al. (2009), where increasing low-level inflow above the boundary layer leads to convergence of angular momentum between 40 to 60 km.

To summarize, the four passes with triple Doppler analysis have shown the detailed convective and kinematic structure and evolution during the weakening stage of an ERC. The analysis points out several important features in the context of an ERC process. First, the analysis suggests that the decay

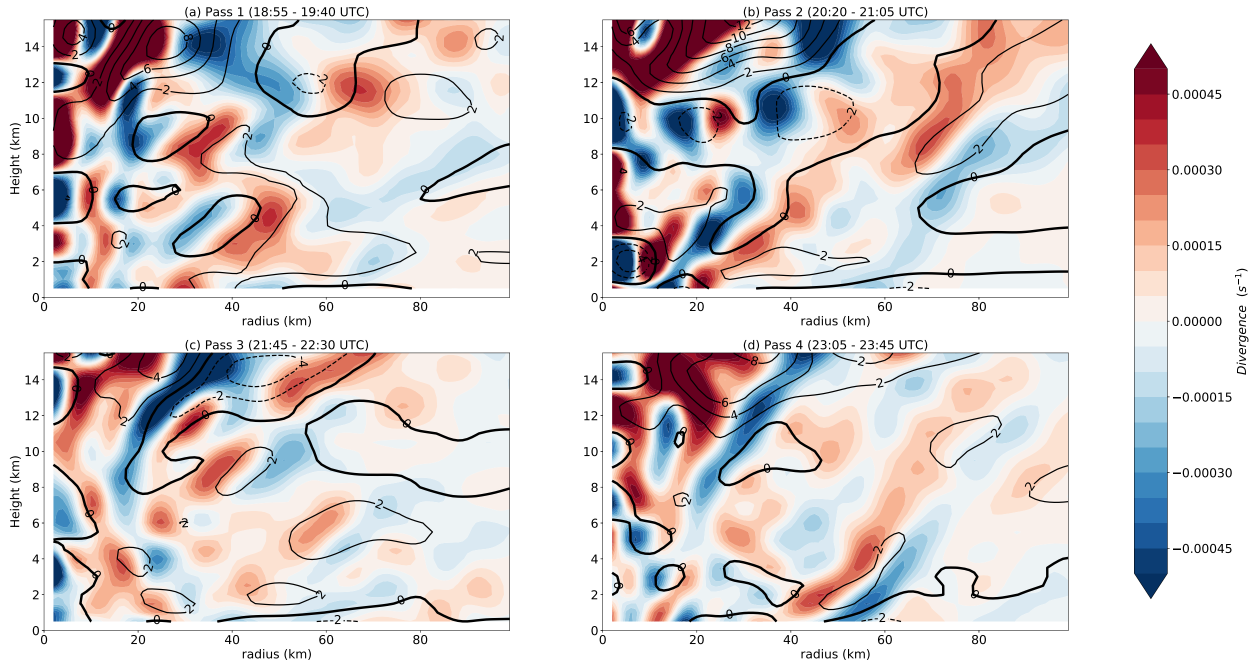


FIG. 3.8. Azimuthally-averaged divergence (shaded, $s^{-1}$) and radial wind (black contour, $ms^{-1}$) derived from P-3 tail radars. Thick black contour highlights azimuthally-averaged radial wind of 0 $ms^{-1}$. (a) Pass 1 (18:55 - 19:40 UTC) (b) Pass 2 (20:20 - 21:05 UTC) (c) Pass 3 (21:45 - 22:30 UTC) (d) Pass 4 (23:05 - 23:45 UTC)

of the inner eyewall was due to decrease in the radial inflow, while the low-level convergence and radial inflow increased at the outer eyewall as it matured. Second, changes in the moat are among one of the most prominent characteristics in ERC evolution. The moat signature disappeared as the secondary circulation of the inner eyewall weakened, and filled with stratiform precipitation. Third, the development of the outer eyewall was observed through the expansion of tangential wind, associated with convergence of angular momentum surfaces and low-level radial inflow, consistent with the first mechanism proposed by Smith et al. (2009).

### 3.2.2 Single Doppler analysis

The single Doppler analysis was from 19 UTC 6 October to 00 UTC 8 October, using KAMX, KMLB, and KJAX observations. During this period, the intensity of Matthew steadily dropped from Category 4 to Category 3, and the environmental shear magnitude increased from 4 $m\,s^{-1}$ to 15 $m\,s^{-1}$. Matthew was more symmetric at the beginning of the analysis period and evolved into an asymmetric storm with an inner and outer eyewall. The inner eyewall was replaced by the outer eyewall while the outer eyewall continued to contract. Figure 3.9 displays the plan view of reflectivity evolution at constant altitude, and Figure 3.10 shows the corresponding vertical cross sections of wavenumber 0 tangential wind. At 1930 UTC 6 October (Figs. 3.9a and 3.10a), the developing outer eyewall was roughly 70 km away from the eye, while the inner eyewall was associated with a nearly circular ring of convection where the strongest reflectivity was located in the downshear left quadrant while the maximum reflectivity of the outer eyewall was located in the upshear left, consistent with the observations in Hence and Houze (2012) and Didlake et al. (2017). The CAPPI reflectivity evolution of the inner eyewall suggest that the new cells periodically formed in the downshear right quadrant, and the cells dissipated in the upshear left quadrant, consistent with previous observations (Reasor et al. 2009). The moat was largely convection-free, which was bounded by the deep convection of the eyewall and developing outer eyewall. The axisymmetric tangential wind derived from single Doppler analysis mostly resembled the azimuthally-averaged tangential wind in pass 1 of the triple Doppler analysis, associated with the intense primary circulation in the inner eyewall region and the signature of a developing outer eyewall. The wind field below the altitude of 3 km cannot be retrieved due to the distance from the radar.

By 0729 UTC 7 October, the maximum reflectivity in the inner eyewall decreased, and the inner eyewall became asymmetric and weak (Fig. 3.9b). Both the maximum of reflectivity of the relict eyewall and outer eyewall were concentrated on the northeast side, suggesting that vertical wind shear played an important role in modulating the storm's structure. Figure 3.10b shows that the axisymmetric primary circulation of the inner eyewall decayed, while the axisymmetric primary circulation of the outer eyewall intensified, associated with a broadening tangential wind field from the radius of 40 to 60 km.

When the relict inner eyewall merged with the contracting outer eyewall (during 13 UTC to 14 UTC 7 October), the radius of the eye expanded and the convection evolved into a semi-circle concentrated on the north side. The wavenumber 0 tangential wind evolved into a slightly tilted tower extending to the altitude of 8 km, suggesting the storm intensified after the inner eyewall disappeared (Figs 3.9c and 3.10c). Figures 3.9d and 3.10d shows that the new eyewall continued contracting but the tangential wind tower decayed. Although the intensity from best track (Fig. 3.1) had a weakening trend, Matthew had retained the Category 3 intensity throughout the whole analysis period and was still a major hurricane.

Changes in convective and kinematic structure have been one of the most prominent indicators of eyewall replacement. Figure 3.11 shows the wavenumber 0 reflectivity, tangential wind, and absolute vorticity temporal evolution at the altitude of 3 km. From Fig. 3.11a, the wavenumber 0 reflectivity intensity of the inner eyewall gradually weakened, and vanished at 0630 UTC 7 October after the

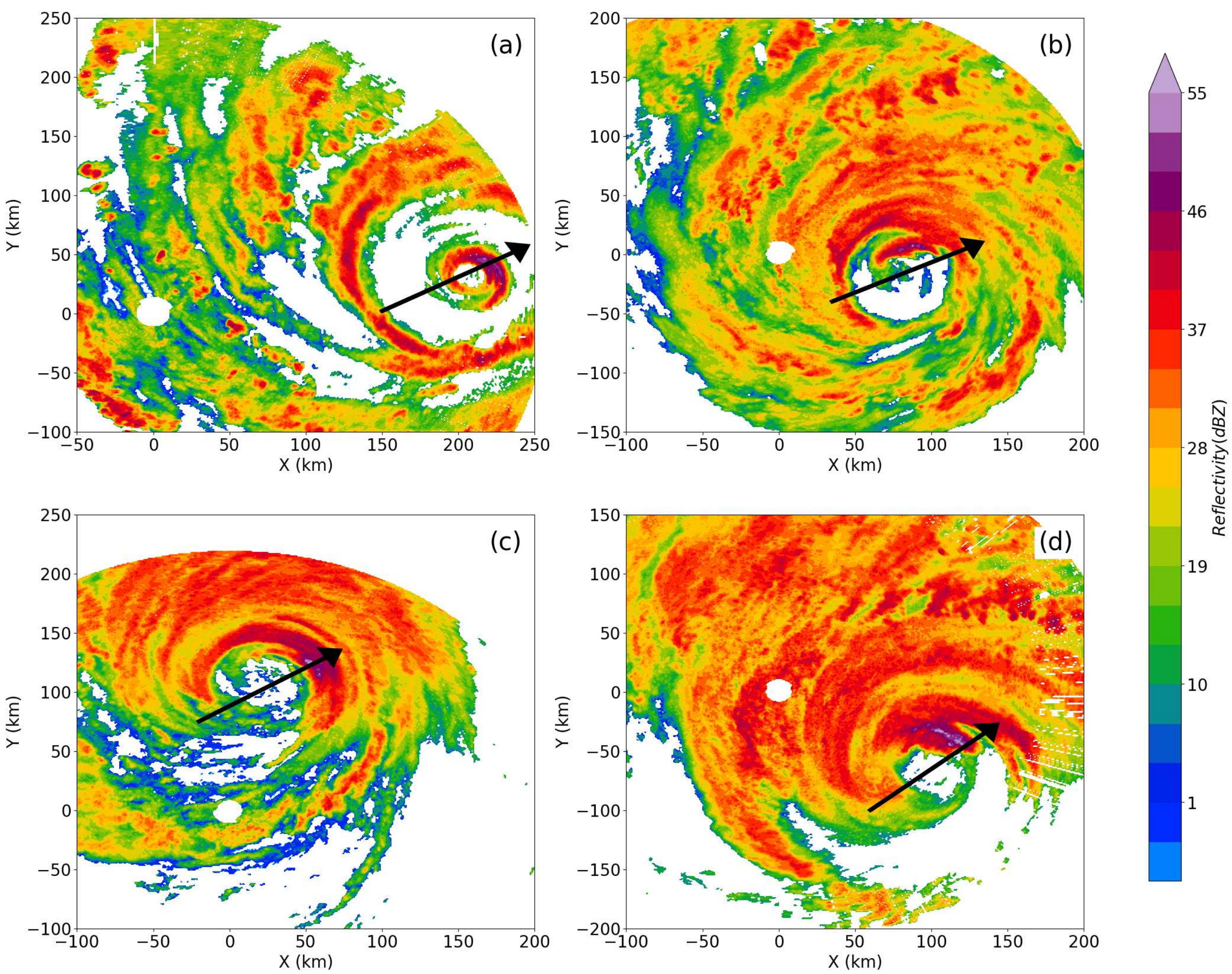


FIG. 3.9. Constant altitude PPI (CAPPI) of reflectivity (a) KAMX radar at 1930 UTC 6 October at 4 km (b) KMLB radar at 0729 UTC 7 October at 3 km (c) KMLB radar at 1400 UTC 7 October at 3 km (d) KJAX radar at 2126 UTC 7 October at 3 km. Black arrow denotes the environmental vertical wind shear direction from SHIPS database.

maximum tangential wind was taken over by the outer eyewall, where the radius of maximum wind increased with a jump from 20 km to 52 km at 0330 UTC 7 October. The moat region was located between 30 - 50 km originally, but diminished afterwards, which is consistent with the triple Doppler analysis. On the other hand, the outer eyewall contracted from the radius of 70 km at 1930 UTC 6 October to 40 km at 1530 UTC 7 October. The contraction rate of the outer eyewall is $1.5\,\mathrm{km\,h^{-1}}$, which is similar to the composite value of $1.75\,\mathrm{km\,h^{-1}}$ in Sitkowski et al. (2011). Note that the wavenumber 0 reflectivity component of the outer eyewall decayed from 1030 to 1230 UTC 7 October, and hereafter reintensified as the inner eyewall merged with the outer eyewall, suggesting that the outer eyewall may have axisymmetrized the asymmetric relict inner eyewall.

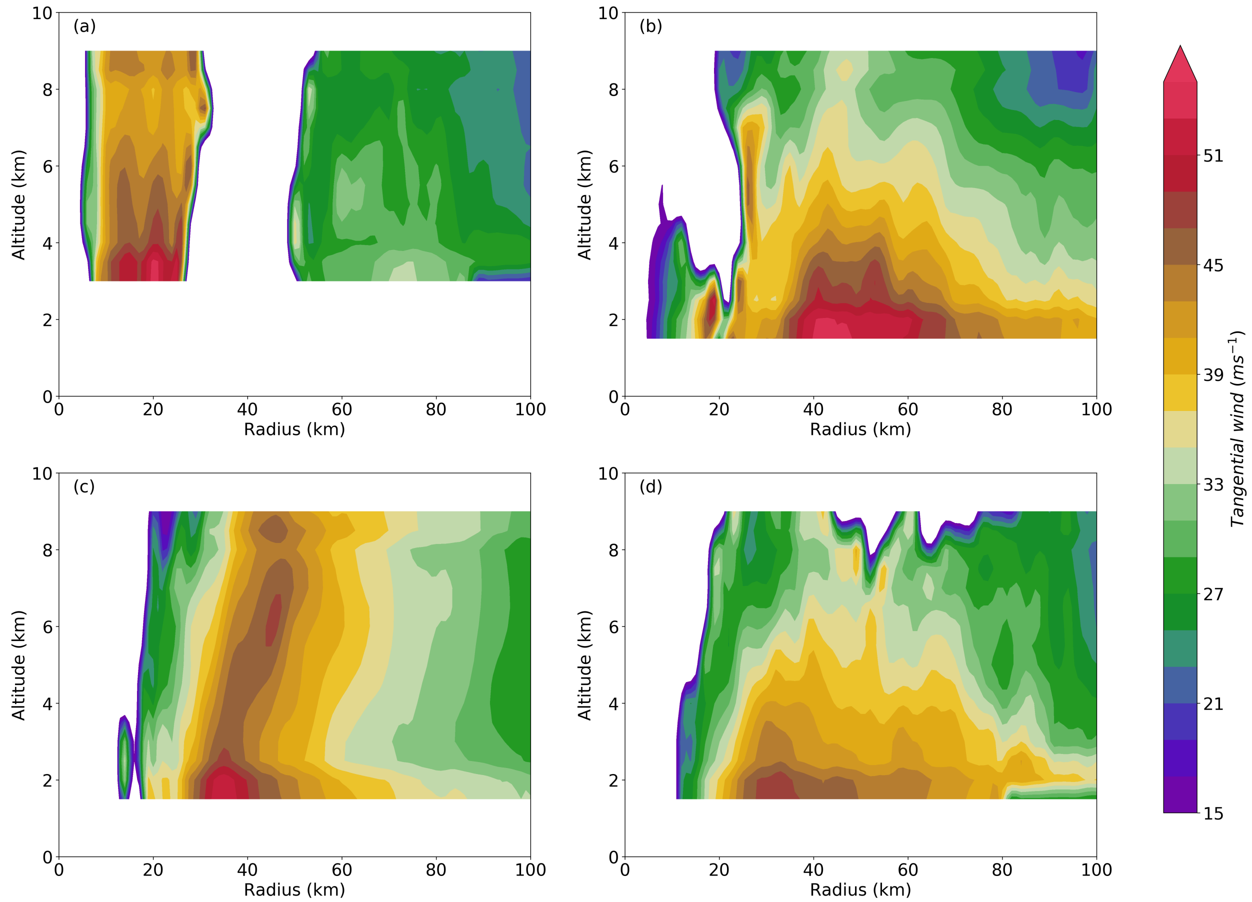


FIG. 3.10. Cross section of wavenumber 0 tangential wind (a) KAMX radar at 1930 UTC 6 October (b) KMLB radar at 0729 UTC 7 October (c) KMLB radar at 1400 UTC 7 October (d) KJAX radar at 2126 UTC 7 October.

Comparing Fig. 3.11a to Fig. 3.11b, it clearly shows that the intensification of the wavenumber 0 tangential wind of the outer eyewall is associated with a weakening intensity of the reflectivity. The different evolution might be because the level chosen here is 3 km. The TC center was distant from the radar in the early period, but the tangential wind typically starts to build up in the lower levels, that aren't detected by the radar. The radially broadening of tangential wind of the outer eyewall in Matthew was clearly captured as the moat disappeared, which is consistent with the triple Doppler analysis. The wavenumber 0 tangential wind in the outer eyewall gradually contracted with fluctuated intensity, and reached a maximum value (55 $\mathrm{m\,s^{-1}}$) when the inner eyewall merged with the outer eyewall (1230 - 1400 UTC 7 October), and then decayed, similar to the axisymmetric reflectivity evolution.

Broadening of the tangential wind field is one of the common features associated with an ERC event. The tangential wind in the outer eyewall region above 40 $\mathrm{m\,s^{-1}}$ extended from the radius of 30 km to 70 km after 0430 UTC 7 October, indicating that the area of damaging winds grew in size. To

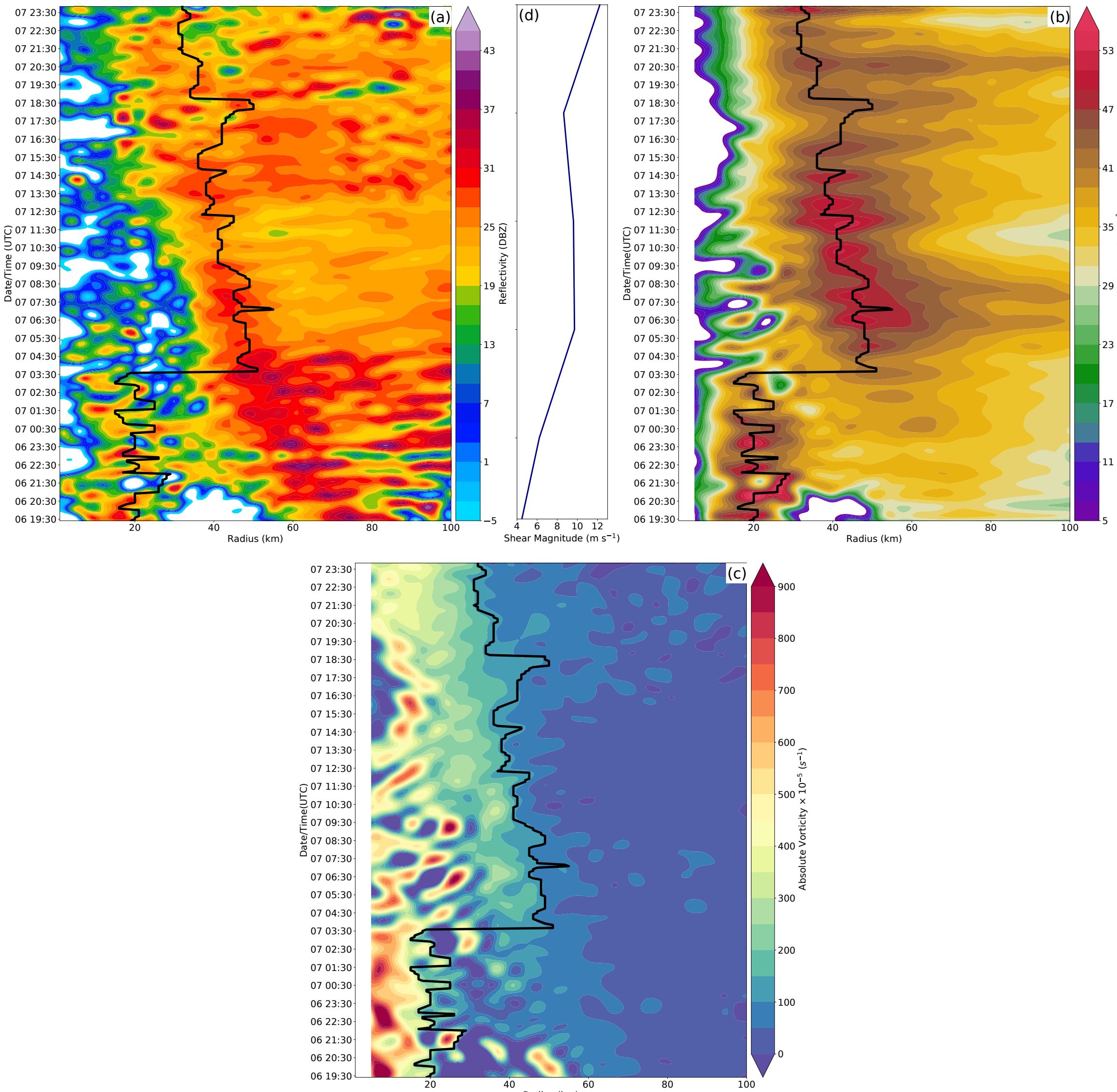


FIG. 3.11. Time/radius diagram of axisymmetric (a) reflectivity (b) tangential wind (c) vorticity from KAMX, KMLB and KJAX radars at altitude of 3 km from 1930 UTC 6 October to 0 UTC 8 October. Black line denotes axisymmetric radius of maximum wind. (d) Shear magnitude evolution from SHIPS database in the same period.

quantify the effect of the expansion of tangential wind, integrating the axisymmetric tangential wind component of kinetic energy $\int_0^{125}[\rho(v^2)/2]dr$ from the center to 125 km radius at the altitude of 3 km shows that the integrated kinematic energy increased 21% from 2030 UTC 6 October to 0830 UTC 7 October. Despite the decay of intensity during this time, Matthew increased in size, resulting in a larger damage swath. After the inner eyewall disappeared, Hurricane Matthew continued weakening rather than undergoinng the reintensification phase, suggesting that the internal dynamics and external forcing influenced the process.

Figure 3.11c reveals that the innermost vorticity maximum exceeded $9 \times 10^{-3}\ \mathrm{s}^{-1}$ in the beginning of the analysis period, and the vorticity profile across the eye and eyewall became broader and flatter after the outer wind maximum surpassed the inner wind maximum. The outermost vorticity maximum in the secondary eyewall region near the radius of 60 km emerged in the early period, located near the inner edge of axisymmetric tangential wind. The radius of maximum wind continued contracting and roughly followed the radial gradient of vorticity. Near the end of the analysis period, the innermost vorticity maximum was less than $5 \times 10^{-3}\ \mathrm{s}^{-1}$, and was associated with weakening axisymmetric components of tangential wind and reflectivity.

## 3.3 Asymmetric Structure and Evolution

The evolution of wavenumber 1 reflectivity and tangential wind fields are shown in Figs. 3.12a and 3.12b. In the beginning of the analysis period, the maximum magnitude of wavenumber 1 reflectivity was over $40\ \mathrm{m\,s^{-1}}$, which had already surpassed the maximum magnitude of axisymmetric component of reflectivity, while the tangential wind was primarily dominated by the axisymmetric component. The wavenumber 1 reflectivity dominated the inner eyewall reflectivity pattern over 8 hours (from 1930 UTC 6 October to 0330 UTC 7 October, Fig. 3.9a). During this same period, the environmental shear was from the southwest and the magnitude increased from 4 to $10\ \mathrm{m\,s^{-1}}$. On the other hand, the outer eyewall structure was dominated by the axisymmetric components, in both reflectivity and tangential wind fields. After the outer wind maximum exceeded the inner wind maximum (0330 UTC 7 October), the outer eyewall reflectivity pattern gradually evolved into an open circle (Fig. 3.9b). The increased wavenumber 1 components suggest that the shear became more influential on the outer eyewall asymmetry than the earlier period.

By 0430 UTC 7 October, the wavenumber 1 reflectivity strengthed gradually, while the wavenumber 1 tangential wind started to increase episodically with a peak value of 10 - $12\ \mathrm{m\,s^{-1}}$ and continued contracting for the next 16 hours. The shear magnitude was moderate between 9 - $11\ \mathrm{m\,s^{-1}}$ at this time. In Reasor et al. (2004), they proposed a conceptual model for the resiliency of a vortex impacted by the vertical shear flow. Although this conceptual model has not been dicussed or observed in an ERC process before, the episodic increases of wavenumber 1 tangential wind of the outer eyewall in here are hypothesized to be a result of the interaction between the shear and the vortex. Therefore, we will mainly focus on the outer eyewall region in the upcoming discussion.

To track the outer eyewall azimuthal evolution, Figure 3.13 shows the azimuthal distribution of wavenumber 1 averaged over the radial bands between RMW - 2 km to RMW + 2 km from 0630 to 2330

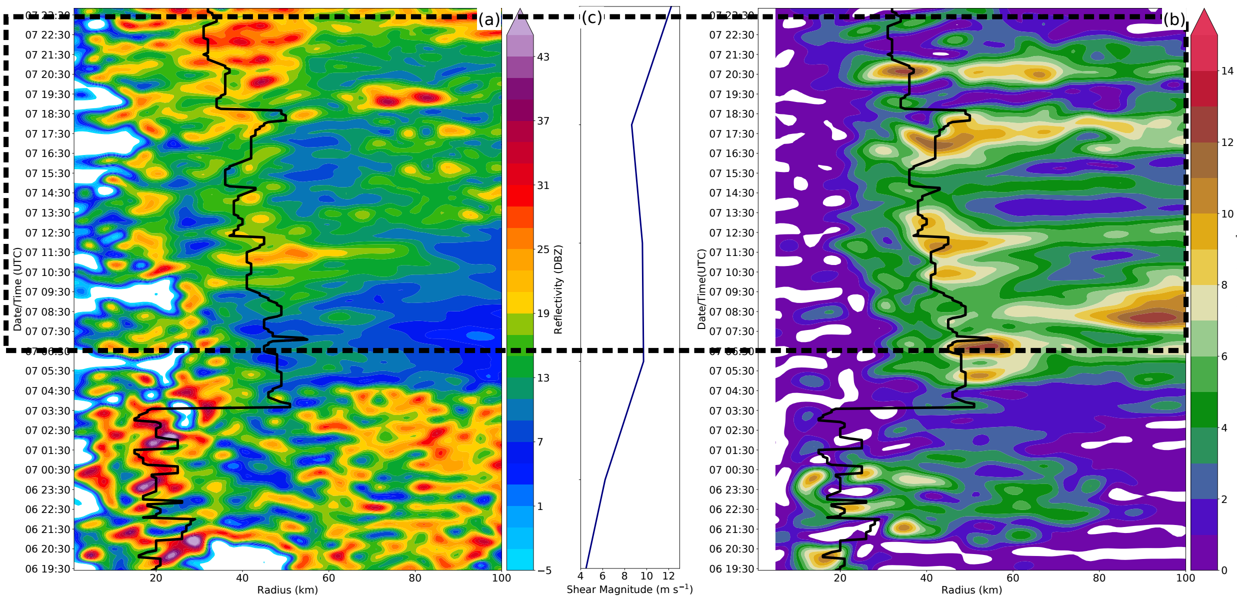


FIG. 3.12. Time/radius diagram of wavenumber 1 (a) reflectivity (b) tangential wind from KAMX, KMLB and KJAX radars at altitude of 3 km from 1930 UTC 6 October to 0 UTC 8 October. Black line denotes axisymmetric radius of maximum wind. (c) Shear magnitude evolution from SHIPS database in the same period. The black dotted box marks the period that will be shown in Figs. 3.13 and 3.14.

UTC 7 October. The shear was moderate at about 10 m s$^{-1}$ and increased to 15 m s$^{-1}$ near the end of observation, and was southerwesterly. The wavenumber 1 reflectivity initially resided in the upshear left quadrant and rotated to the downshear left quadrant, consistent with the result of azimuthal upwind shift for the reflectivity from Didlake et al. (2017). Although Didlake et al. (2017) did not show the azimuthal distribution of tangential wind, Figure 3.13b illustrates that wavenumber 1 tangential wind rotated to downshear left quadrant along with the reflectivity, and the wavenumber 1 reflectivity stayed left of shear for the rest of observations while the tangential wind continued rotating cyclonically and mostly stayed right of shear.

The opposite quadrant of reflectivity (left of shear) and tangential wind (right of shear) suggests the impact of external forcing such as land friction. Although Matthew did not make landfall during our analysis period, the hurricane center was close to the east coast and the storm might interacted with the land. Hence, we suspect that the combination of the internal vortex dynamics, land friction, and shear direction may have played a role in the azimuthal distribution of wavenumber 1 tangential wind.

When the outer eyewall replaced the inner eyewall (6-18 UTC 7 October), the deep layer environmental vertical shear was about 9 - 11 m s$^{-1}$ with a slight reduction of magnitude between 12 - 18 UTC 7 October. Nevertheless, the wavenumber 1 reflectivity and tangential wind both increased during that

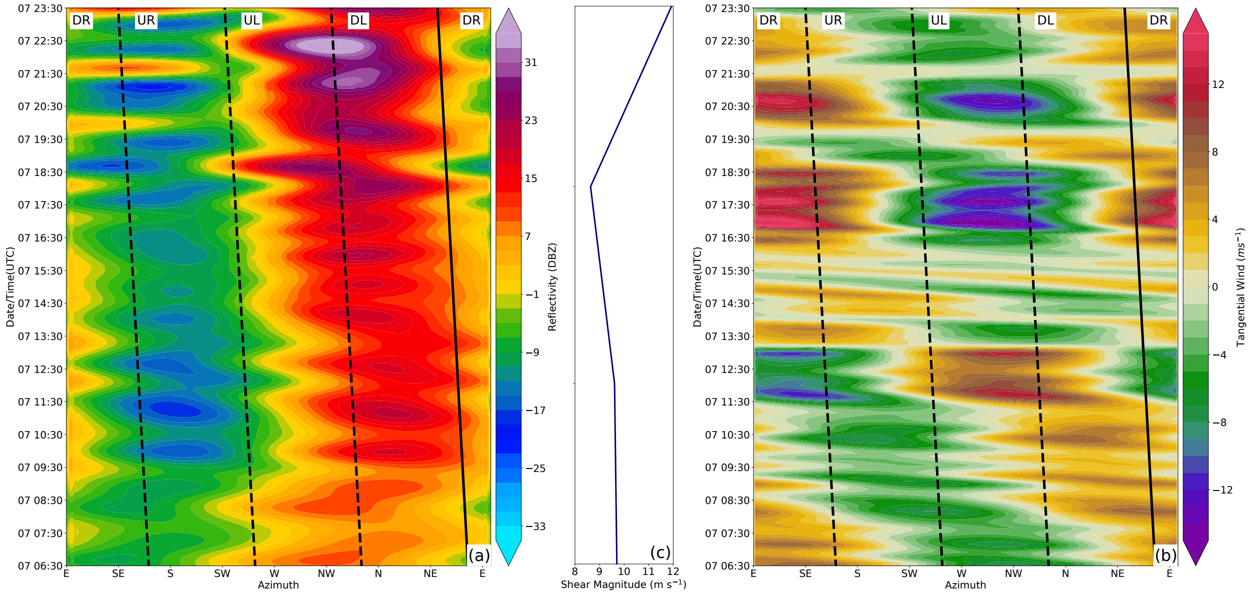


FIG. 3.13. Time/azimuth diagram of wavenumber 1 (a) reflectivity (b) tangential wind averaged between RMW-2 km to RMW+2 km from the center of Matthew with KMLB and KJAX radars at altitude of 3 km from 0630 UTC to 2330 UTC 7 October. Thick black line denotes the shear direction interpolated from SHIPS database. (c) Shear magnitude evolution from SHIPS database in the same period.

time. Although the environmental shear derived from the SHIPS database might not be consistent with the local shear, there is a possibility that internal vortex mechanism such as the propagation of VRW can reduce the asymmetry. As the shear intensified rapidly later on, the vortex structure was associated with prominent wavenumber 1 asymmetries. The interaction between internal vortex dynamics and shear dynamics have had a significant impact on Matthew's evolution.

As the radar images (Fig. 3.9b and c) have shown before, Matthew's outer eyewall exhibited noncircular shapes. Those features have been discussed in previous studies (Kuo et al. 1999; Corbosiero et al. 2006), indicating the importance of internal vortex interaction. The propagation of VRW can transport momentum and relax the vorticity gradient. When the VRW interacts with a sheared vortex, the damping mechanism of VRW can yield to a resilient vortex. If it continues to interact, this damping mechanism can yield to a realignment of vortex. The estimation of VRW propagation speed is consistent with the wave propagation theory which $C_\lambda = V_{max}(1-1/n)$, where n is the azimuthal wavenumber (Lamb 1932). The wavenumber 2 rotation rate will be nearly half of the maximum tangential speed (Kuo et al. 1999).

Figures 3.14a and b show the wavenumber 2 azimuthal evolution of reflectivity and tangential wind tracked by the radius of maximum wind and averaged over 5 km radial bands. Both wavenumber 2 tangential and reflectivity components stayed in the same quadrant between 0630 to 0730 UTC 7 October.

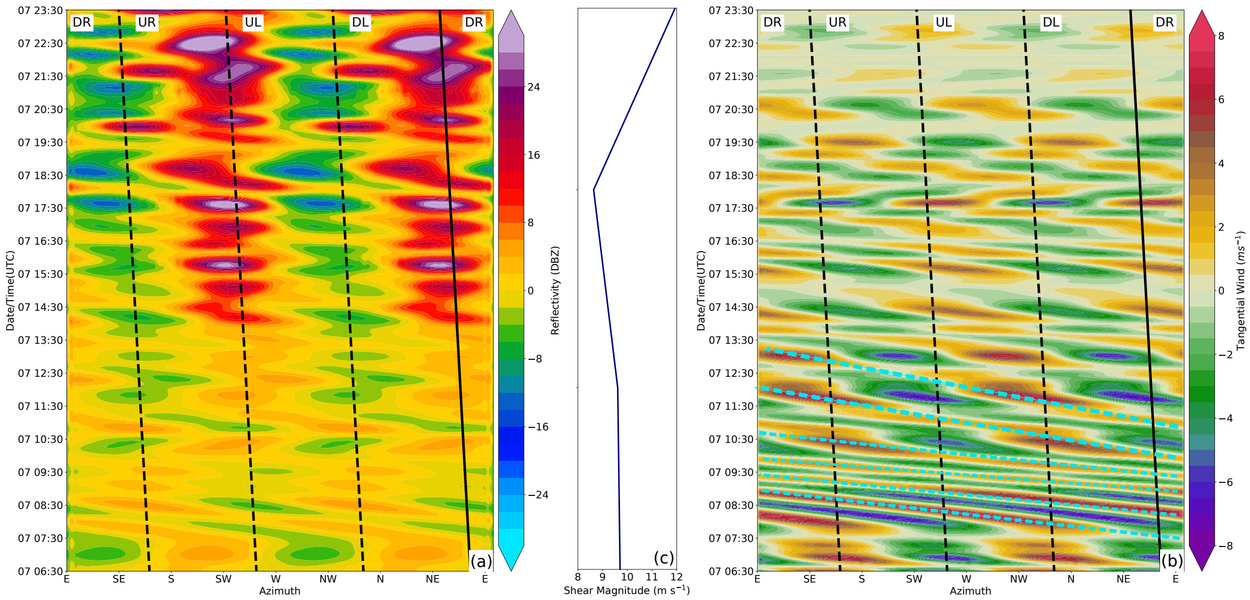


FIG. 3.14. Time/azimuth diagram of wavenumber 2 (a) reflectivity (b) tangential wind averaged between RMW-2 km to RMW+2 km from the center of Matthew with KMLB and KJAX radars at altitude of 3 km from 0630 UTC to 2330 UTC 7 October. Thick black line denotes the shear direction interpolated from SHIPS database. (d) Shear magnitude evolution from SHIPS database in the same period.

The positive wavenumber 2 component of tangential wind was mostly collocated with reflectivity from 0730 to 1130 UTC and completed four full azimuthal rotations, and continued rotating cyclonically while the wavenumber 2 reflectivity mostly stayed in the same quadrant for the rest of time. The cyan colored line in Fig. 3.14b follows the azimuthal rotation of the bands. They were used to calculate the azimuthal phase speed, and the propagation speed between 1130 and 1330 UTC was 36.65 m s$^{-1}$ at approximately a radius of 42 km. The retrieved phase speed is about 58 % of the total tangential wind (wavenumber 0 + wavenumber 1 + wavenumber 2), consistent with the VRW theory. The cyclonic propagation of the wavenumber 2 tangential wind was prominent between 1330 - 1730 UTC 7 October, while the wavenumber 1 tangential wind slightly weakened between 1330 - 1530 UTC and reintensified afterwards when the shear started to increase.

As the shear increased rapidly near the end of observation, the storm was apparently dominated by the wavenumber 1 component (Fig. 3.9c and d). The propagation of wavenumber 2 tangential wind component weakened and stayed in the same quadrant as a result of the intensifying shear, and the magnitude became smaller in the tangential wind field but stronger in the reflectivity field. The reason for this inconsistent pattern between wavenumber 2 reflectivity and tangential wind is uncertain. One explanation could be due to the limitations of the GVTD retrieval method. The retrieved wavenumber

2 tangential wind neglected the wavenumber 2 radial wind and higher order terms when constructing the tangential wind (Eqs. 2.18 and 2.19). If the wavenumber 2 radial wind increases, it would introduce the uncertainty to the retrieved wavenumber 2 tangential wind. The other significant pattern is that wavenumber 2 reflectivity was not necessarily collocated with wavenumber 2 tangential wind for the entire period (Fig. 3.14a and b), consistent with the modeling work of Moon and Nolan (2015).

The vortex realignment process cannot be fully diagnosed because of the limitations of the dataset. Nonetheless, the analyses document that the ERC evolution appears to be impacted by the interaction between the shear and the internal VRWs, and suggest that the vortex resiliency conceptual model from Reasor et al. (2004) may be applicable. The lack of the reintensification phase was caused by the increasing shear.

# CHAPTER 4

## Comparison of wind retrievals between single Doppler and triple Doppler analyses

### 4.1 Examine the performance of GVTD technique with triple Doppler analysis

Both Lee et al. (1999) and Jou et al. (2008) have tested the GBVTD and GVTD technique respectively with analytic datasets and confirmed the reliability of these two methods. However, none of the previous studies have conducted a detailed comparison of the Fourier decomposition of the wind field between single Doppler and multi-Doppler retrieval. Therefore, our triple Doppler analysis with three-dimensional wind retrieval would be optimal to evaluate the performance of the GVTD technique if the wind field from triple Doppler analysis is treated as the truth. Although the retrieved wind field might not be perfect, assuming the retrieved wind field from triple Doppler analysis as the truth ensures the comparability of the wind field. All constructed coeffecients (Eqs. 2.15 to 2.19) can be composed by the Fourier decomposition of $V_T$ and $V_R$ from the triple Doppler analysis, known storm motion and mean wind components. To test the single-Doppler retrieval, the wind field from the triple Doppler analysis was resampled into Doppler velocity observed by KAMX radar and then we performed the GVTD at the radius of maximum wind (18 km) in the inner eyewall region from pass 1 (1855 - 1940 UTC 7 October), where the storm center is centered at 1920 UTC 6 October.

Figure 4.1 shows the comparison of constructed coefficients and retrieved coefficients with the GVTD technique. The retrieved coefficients match nearly perfectly with the constructed coefficients and only a slight deviation is observed. The deviation is probably some artificial signals from the linear least square method trying to fit the velocity on a ring. Although we only test a single case, the above result confirms that the GVTD technique can qualitatively and quantatively retrieve the wind field, providing insightful TC kinematic structure with ground-based single Doppler radar data.

### 4.2 Examine the performance of improved-GVTD algorithm with single Doppler analysis and triple Doppler analysis

In Chapter 2, we improved the GVTD algorithm by separating the storm motion from the mean wind component, where the result is displayed in Fig. 4.2. Each dot represents the intensity of wavenumber 0 tangential wind at a radius. Blue dots were retrieved by Fourier decomposition of tangential wind with the triple Doppler analysis, orange dots were retrieved by the original GVTD algorithm with the single Doppler analysis, and red dots were retrieved by the improved GVTD algorithm

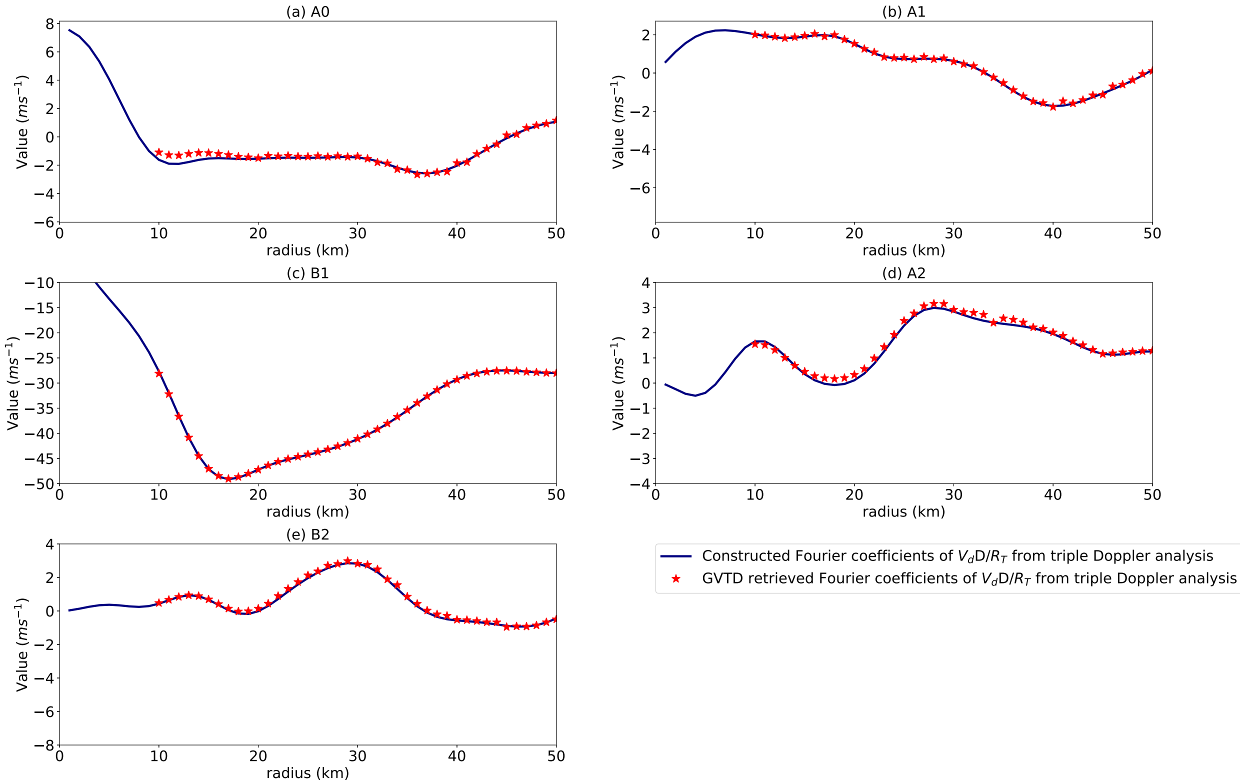


FIG. 4.1. The comparison of $V_d D/R_T$ Fourier coefficients between constructed coefficients (based on the Fourier decomposition of $V_T$, $V_R$, known storm motion, and mean wind) and retrieved coefficients from triple Doppler analysis pass 1. The blue line denotes the construced coefficients, and the red star denotes the retrieved coefficients. The least square fit of $V_d D/R_T$ is at the radius of 18 km.

with the single Doppler analysis. Since the GVTD technique neglects the asymmetric components of radial wind, the wavenumber 0 tangential wind derived from the triple Doppler analysis is more reasonable to be assumed as the truth. The wavenumber 0 components retrieved from different method have similar magnitude from the radius of 10 to 30 km, suggesting that the axisymmetric tangential wind retrieve from each platform is in good agreement. The storm motion has relatively small impact on the intensity of wavenumber 0 in the inner core because $R/R_T$ is small. On the contrary, as the radius increases, the storm motion term becomes relatively impactful on the estimation of wavenumber 0 tangential wind. Between the radius of 40 to 70 km, the deviation between the analyses becomes larger, while the single Doppler analysis with the improved GVTD algorithm is more consistent with the triple Doppler analysis compared to the original GVTD algorithm. The maximum deviation can be up to 3 - 4 $\mathrm{m\,s^{-1}}$. In this case, the improved GVTD algorithm with storm motion can have a more accurate estimation of the wavenumber 0 tangential wind intensity.

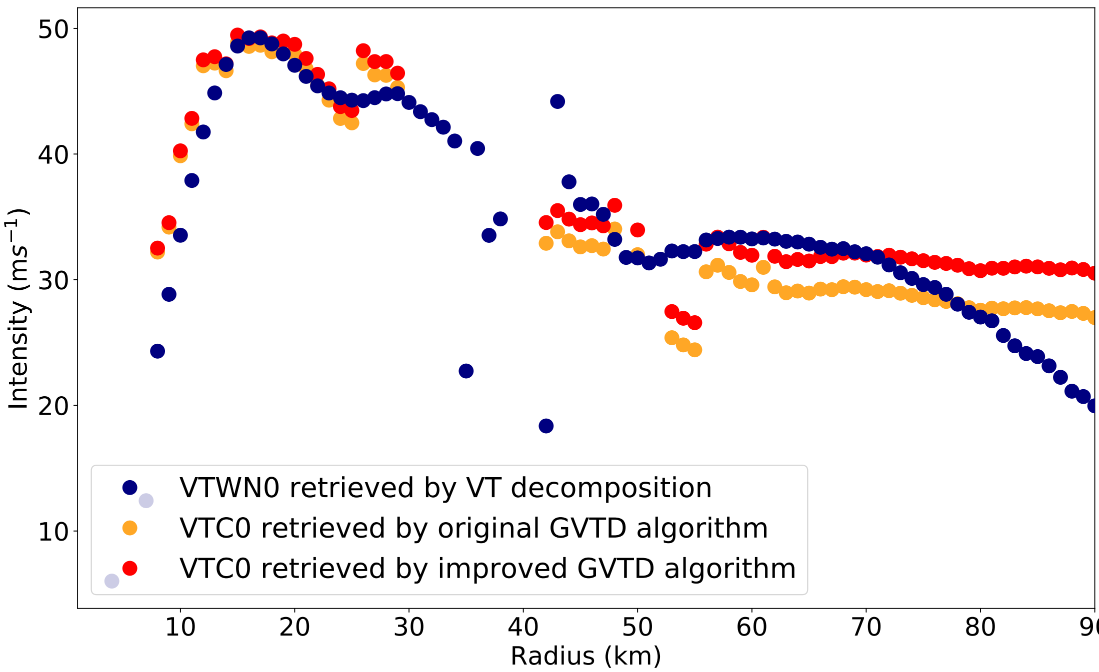


FIG. 4.2. Wavenumber 0 tangential wind is retrieved respectivity by Fourier decomposition of tangential wind from the triple Doppler analysis (blue dots), original GVTD algorithm from the single Doppler analysis (orange dots), and improved GVTD algorithm from the single Doppler analysis (red dots).

### 4.3 Compare the performance of GVTD technique with single Doppler analysis and triple Doppler analysis

With the confidence of the performance of GVTD technique, the next step is to examine the applicability of a steady-state assumption of the triple Doppler analysis. Following the section above, the wind field from the triple Doppler analysis was resampled into Doppler velocity observed by KAMX radar. Figure 4.3 shows the Doppler velocity observed by KAMX radar and Doppler velocity projected from triple Doppler analysis. The maximum Doppler velocity of single Doppler analysis is not collocated with the maximum Doppler velocity of triple Doppler analysis. The single Doppler observations have much more missing data in the inner core region due to the longer range from the radar and contamination with other factors. To quantitatively compare, we examine the data in the radius of maximum wind (18 km) within the inner eyewall region denoted by the dashed black countour.

Figure 4.4 shows the Fourier coefficients of $V_d D/R_T$ from the triple Doppler and single Doppler analyses. In general, A0, A1 and B1 coefficients from the single Doppler analysis are in a good agreement with triple Doppler analysis with small deviations (less than 2 m s$^{-1}$) within the eyewall region. The coefficients possess larger deviation from the eye to the inner edge of eyewall and outside of the

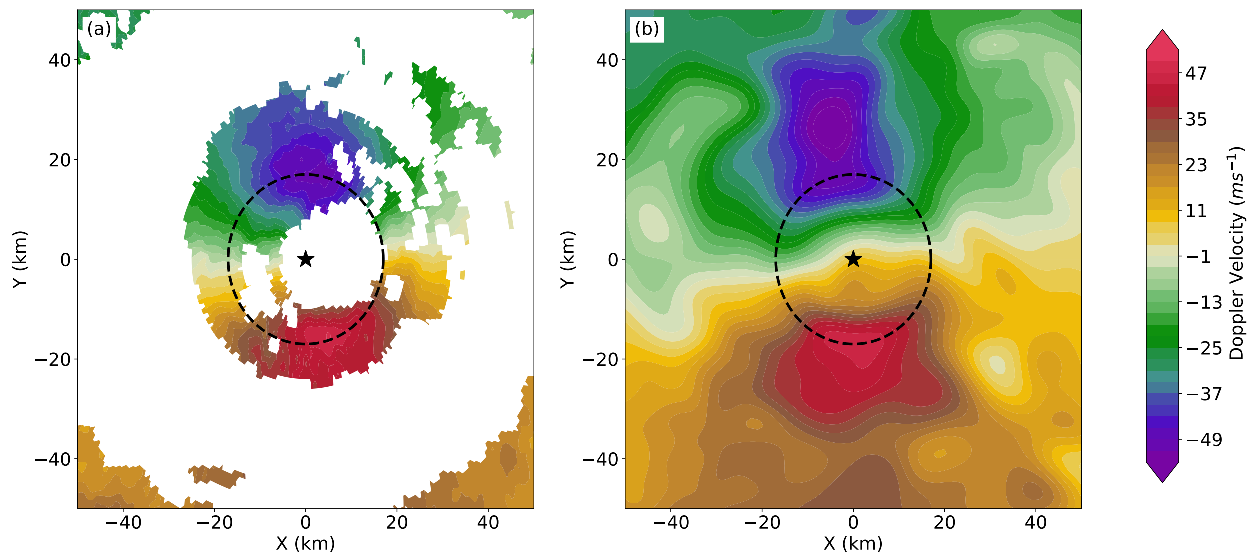


FIG. 4.3. The Doppler velocity observed by KAMX obtained from (a) KAMX radar (b) triple Doppler analysis. The black star denotes the radar location, and the dashed circle denotes the radius of maximum wind (18 km) estimated from GVTD analysis.

eyewall region. The deviation might be due to the density of data coverage, where the airborne analysis has high spatial resolution and is able to capture much more detail, but the single Doppler observation has a poor data coverage and might be contaminated by noise. A0, A1, and B1 from both analyses are mostly in the same phase (both positive or both negative). Interestingly, A2 and B2 possess larger discrepancy, and especially B2 is totally out of the phase between two retrievals. Both A2 and B2 from triple Doppler analysis have smaller amplitude than A2 and B2 from single Doppler analysis, suggesting the mismatch pattern of wavenumber 1 tangential wind (Eq. 2.19). This results implies that the phase and magnitude of wavenumber 1 tangential wind would be different, and confirms the concern from Lee et al. (1994) discussed before.

Figure 4.5a displays the $V_d D/R_T$ derived from triple Doppler and single Doppler analyses. It shows that the $V_d D/R_T$ from both analyses are clearly dominated by wavenumber 1 pattern, which confirms the similarity of retrieved coefficients magnitude in A1 and B1 (Fig. 4.4). In this case, the retrieval of wavenumber 0 tangential wind, radial wind, and mean wind component should have comparable magnitude in both analyses. However, there is a slight deviation in the phase, suggesting that higher wavenumbers might play an important role in determining the discrepancy. Therefore, Figure 4.5b shows the residuals after the substraction of wavenumber 0 and wavenumber 1 components of $V_d D/R_T$ from total $V_d D/R_T$. The residuals include wavenumber 2 and higher wavenumber components. It shows that the residuals from the single Doppler analysis are dominated by the wavenumber 2

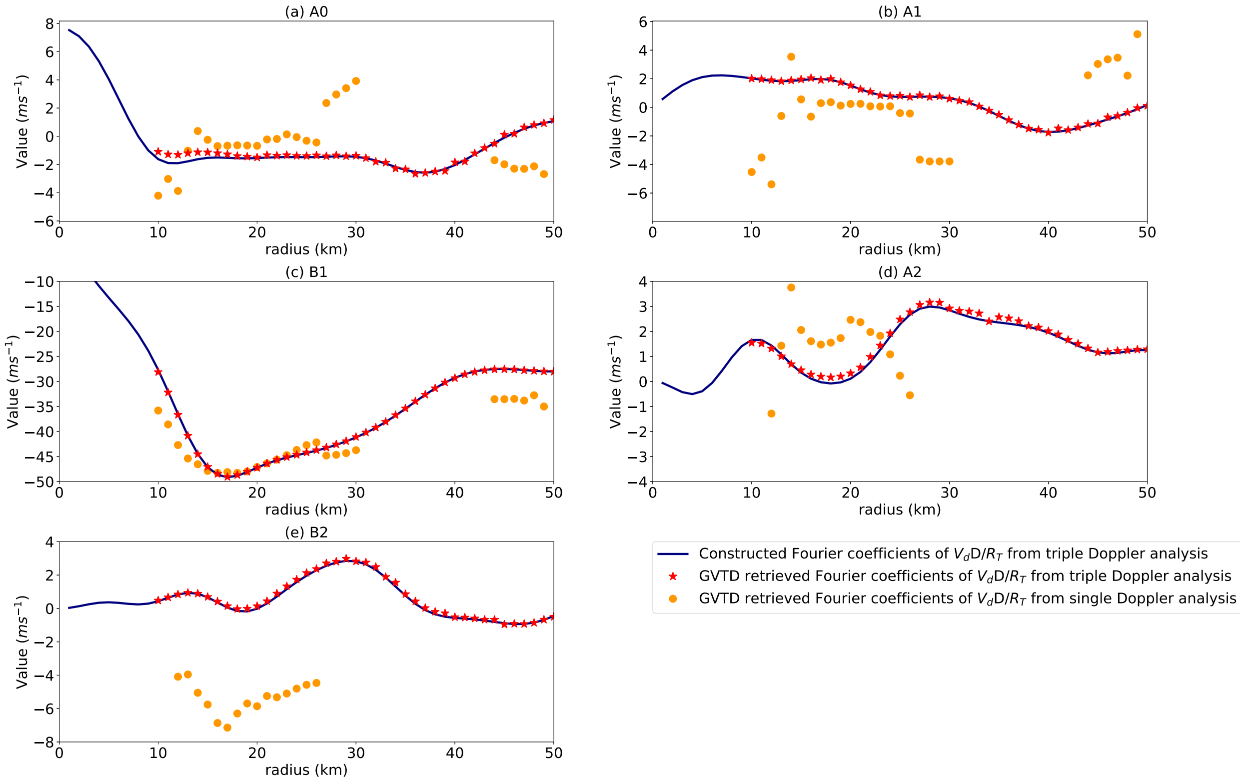


FIG. 4.4. The comparison of $V_d D/R_T$ Fourier coefficients between constructed coefficients (based on the Fourier decomposition of $V_T$, $V_R$, known storm motion, and mean wind), retrieved coefficients from triple Doppler analysis pass 1, and retrieved coefficients from KAMX radar at 1921 UTC 6 October. The blue line denotes the construced coefficients, and the red star denotes the retrieved coefficients. The least square fit of $V_d D/R_T$ is at the radius of 18 km.

component, while the residuals from the triple Doppler analysis are noisy and without a clear pattern. The peak value of the residual from the single Doppler analysis is 8 $\mathrm{m\,s^{-1}}$, but the peak value of the residual from the triple Doppler analysis is about 2.5 $\mathrm{m\,s^{-1}}$. This result illustrates that the wavenumber 1 tangential wind retrieval between two analyses is different due to the difference in the wavenumber 2 component of $V_d D/R_T$. The wind synthesis in triple Doppler analysis is broadened and smoothened. Since the accuracy of wind retrieval with GVTD technique has already been demonstrated, we suspect that the mismatch of retrieved wavenumber 1 tangential wind is due to the assumption of steady state in the triple Doppler analysis, which would not be valid with the wavenumber 2 tangential wind as the VRW propagates. Since the propagation speed of a wavenumber 2 VRW is approximately half of the maximum tangential wind, it may alias into wavenumber 1 tangential wind and further mitigate the amplitude of wavenumber 1 tangential wind. Therefore, we hypothesize that the propagation of VRWs can introduce a bias in the triple Doppler analysis.

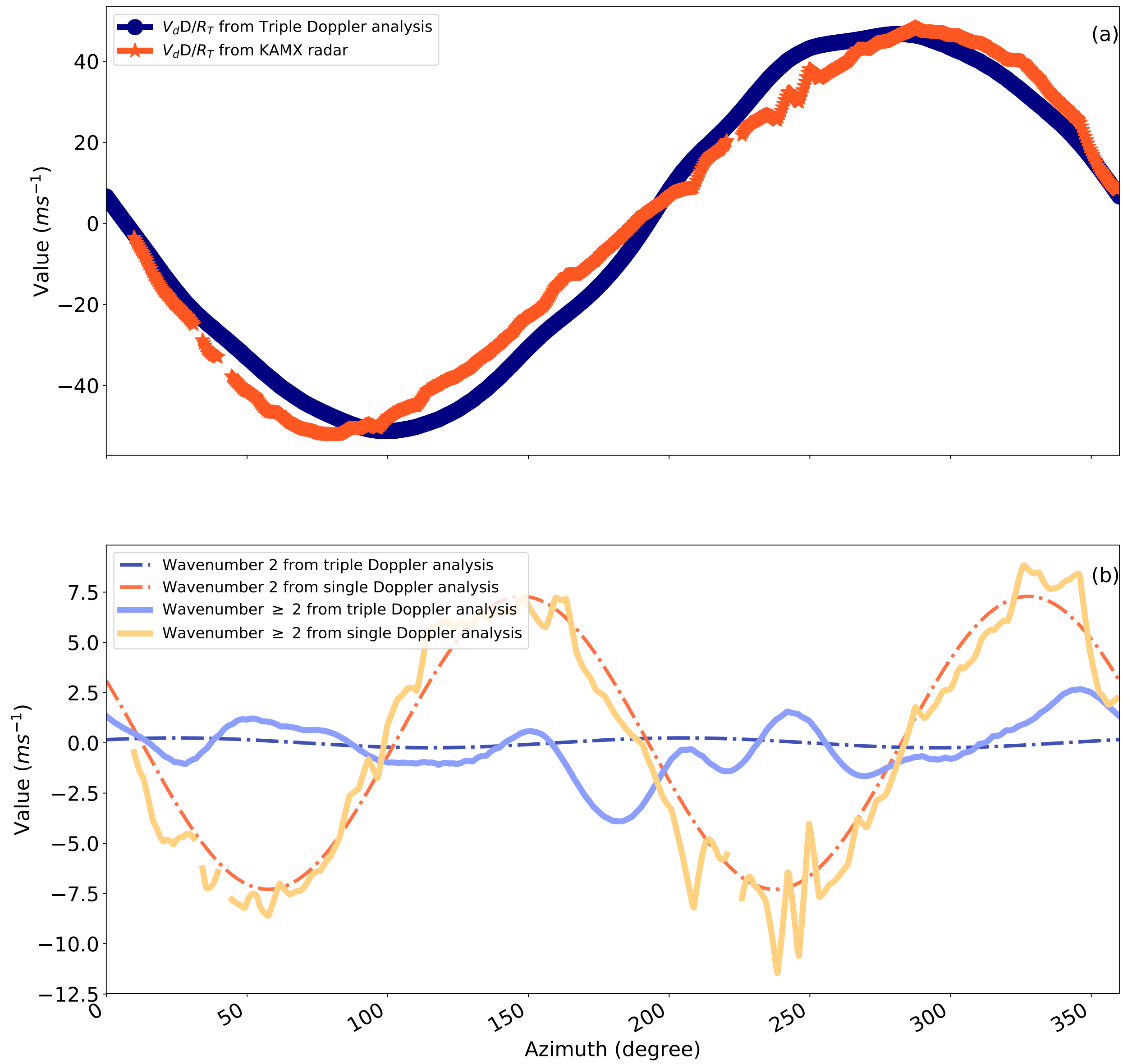


FIG. 4.5. (a) Comparison of retreived $V_d D/R_T$ between triple Doppler and single Doppler analyses. Blue line denotes retreived $V_d D/R_T$ from triple Doppler analysis, and orange line denotes retreived $V_d D/R_T$ from KAMX radar. (b) Comparison of retrieved wavenumber 2 and even higher wavenumber of $V_d D/R_T$ between triple Doppler and single Doppler analyses. The solid line denotes the residuals of subtracting wavenumber 0 and 1 from $V_d D/R_T$. The dash-dotted line represents the wavenumber 2 component of $V_d D/R_T$.

In order to further diagnose this problem, we utilized the phases of wavenumber 1 and wavenumber 2 tangential winds and reflectivity retrieved from the single Doppler observations to examine the temporal evolution within one flight pass (1855 to 1940 UTC 6 October). The phase of tangential wind is derived from $V_T S_N / V_T C_N$, and is similarly calculated for reflectivity. Figure 4.6a and c show the temporal evolution of wavenumber 1 phase in reflectivity and tangential wind respectively. The wavenumber

1 reflectivity and tangential wind were collocated in the downshear quadrant and nearly unchanged for the first 50 minutes, suggesting that the wavenumber 1 distribution is forced by the vertical wind shear. This is consistent with the discussion in Chapter 3. On the other hand, Figure 4.6b and d show the temporal evolution of wavenumber 2 phase in reflectivity and tangential wind respectively. Not surprisingly, both wavenumber 2 reflectivity and tangential wind components propagated azimuthally during the pass 1. The propagation of a wavenumber 2 tangential wind is estimated to be 160 degrees from 1915 to 1945 UTC, which is 31 $\mathrm{m\,s^{-1}}$, or 63% of $V_{T max}$. The propagation of wavenumber 2 tangential wind is roughly consistent with the VRW theory.

If we consider the P3 flight speed as 120 $\mathrm{m\,s^{-1}}$, and the diameter of the eye is 36 km at this time, it would take five minutes for P3 to fly across the inner eyewalls. The flight time implies that a wavenumber 2 VRW had already propagated for 21.67 degrees. Hence, the propagation of wavenumber 2 tangential wind aliased on the steady wavenumber 1 component, so the reduced amplitude and phase shift in A2 and B2 are evident in the triple Doppler analysis compared to the single Doppler analysis. The above analysis supports our hypothesis that the discrepancy in the wavenumber 1 tangential wind between single Doppler and triple Doppler observations is due to the propagation of a wavenumber 2 VRW.

Based on this analysis, performing airborne pseudo-dual Doppler radar analysis requires extra caution. The retrieved mean wind and wavenumber 0 component of tangential and radial winds from the triple Dopple analysis resemble the single Doppler analysis, since the stationary assumption for one flight leg is usually valid for the axisymmetric circulation and mean wind. Nonetheless, the steady-state assumption is not applicable with the presence of short temporal scale activities, such as convective bursts, rotation of mesovortices, and propagation of higher order VRWs. The above factors could potentially reduce the maximum of wind and reflectivity fields derived from the triple Doppler analysis due to spatial and temporal aliasing. Although the result raises concern about the potential acuracy of Fourier decomposition of multiple Doppler analysis, the axisymmetric convective and kinematic structure revealed in the triple Doppler analysis is consistent with the single Doppler analysis (Chapter 3). The pseudo-dual Doppler analysis tends to have substantial impact on low-wavenumber structure unless we consider the time evolution within one flight leg. Future work is required on the time-dependent analysis of asymmetric structure, which is beyond the scope of this study.

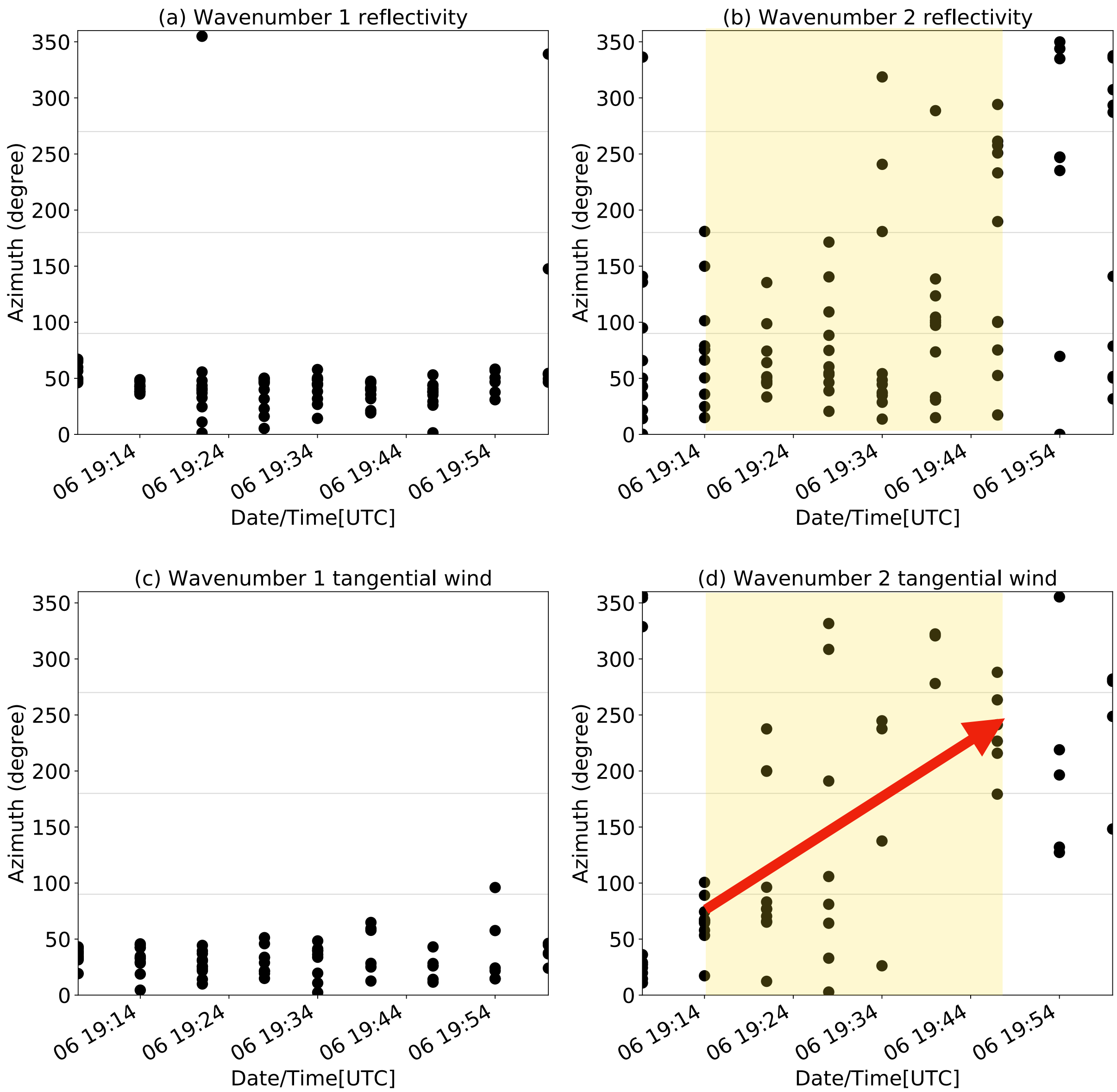


FIG. 4.6. The azimuthal temporal evolution of wavenumber 1 and 2 of reflectivity and tangential wind in the inner eyewall region (from the radius of 15-25 km) from 1900 to 2000 UTC 6 October. The black dots are (a) Wavenumber 1 reflectivity, (b) Wavenumber 2 reflectivity, (c) Wavenumber 1 tangential wind, and (d) Wavenumber 2 tangential wind within the area from the radius of 15 to 25 km. The red arrow denotes the propagation of the median of wavenumber 2 tangential wind from 1915 to 1945 UTC, and the yellow shading illustrates the period of 1915 UTC to 1945 UTC.

# CHAPTER 5

## Conclusion

Analyses of triple Doppler and single Doppler datasets support previous studies of ERCs evolution in axisymmetric framework, and provide new insights into the asymmetric ERC evolution of Hurricane Matthew. The analysis suggests Matthew's ERC evolution is consistent with intensification and weakening of a classic ERC (Sitkowski et al. 2011), but reintensification was never realized due to increasing vertical wind shear. Four passes of triple Doppler analysis shows detailed convective and kinematic evolution of a weakening inner eyewall and a developing outer eyewall. The weakening inner eyewall was associated with a decaying secondary circulation and a clear moat region disappeared through passes, while the strengthening outer eyewall was accompanied by an increasing secondary circulation and a broadening of tangential wind field. The vorticity of the developing outer eyewall was maximized at low levels and closely coupled with low-level inflow and convergence of angular momentum. The development of the outer eyewall supports the first axisymmetric mechanism proposed by Smith et al. (2009) as a well-recognized framework for understanding the intensification.

35-hour single Doppler analysis documents the dissipation of the inner eyewall and contraction of the outer eyewall with increasing asymmetry due to increasing vertical wind shear. The beginning of the observation period shows that the clear moat and concentric eyewall pattern were distinct, suggesting that the secondary circulation of the inner eyewall was still intense. The asymmetries of the inner eyewall increased gradually as the shear increased and merged with the outer eyewall in the later period. When the shear magnitude intensified to around 9-11 $\mathrm{m\,s^{-1}}$, the asymmetries of the outer eyewall increased episodically, suggesting the vortex was resilient to the vertical wind shear. Furthermore, the wavenumber 2 tangential wind field shows evidence of propagating VRWs in the outer eyewall region that suggest internal asymmetric dynamics may have played an important role in the ERC evolution impacted by vertical wind shear. The above results indicate that the vortex resiliency was influenced by both the internal VRW damping mechanism and environmental shear dynamics. On the other hand, the wavenumber 2 reflectivity field was not necessarily collocated with the VRW, which is consistent with Moon and Nolan (2015). When the shear increased rapidly, the asymmetric structure of Matthew was dominated by the shear, and the VRW propagation weakened.

Reasor et al. (2004) proposed that the internal VRW damping mechanism can maintain the vortex vertical alignment in a sheared environment. Doppler analysis of Matthew's outer eyewall evolution suggests that the vortex resiliency conceptual model from Reasor et al. (2004) may be applicable. The results have shown that wavenumber 1 asymmetry was largely forced by the vertical wind shear, and the cyclonic propagation of the wavenumber 2 tangential wind was prominent while the wavenumber 1 tangential wind slightly weakened (1330-1530 UTC 7 October). Nevertheless, the vertical structure of Matthew was not able to be examined in detail due to the limitations of the dataset since the accuracy of GVTD-simplex centers is questionable, which make it difficult to assess the vertical reduction of tilt. The exact processes are still unclear due to the limitations of our dataset. Future examination of how the VRW damping mechanism influences outer eyewall intensity and these dynamical interactions with modeling studies are needed.

Wind retrievals from a single Doppler radar are powerful to monitor TCs kinematic evolution, which has been demonstrated in the previous studies with the GBVTD (Lee et al. 1999; Lee and Marks 2000; Lee and Bell 2007; Zhao et al. 2008) and the GVTD (Jou et al. 2008) techniques. Although the GVTD technique substantially improves the capability of the GBVTD, rare work has conducted it as a research tool instead of the GBVTD. In our study, we utilize the GVTD technique and improve the algorithm of the GVTD technique by separating the storm motion from the mean wind component, which yields a more accurate estimation of mean wind, wavenumber 0 tangential and radial winds. Although the GVTD technique is able to retrieve the kinematic structure of the storm, neglecting the asymmetric components of radial wind to obtain the asymmetric components of tangential wind may be inappropriate when the storm was dominated by the asymmetries, and another closure assumption for GVTD technique is needed to improve the accuracy of the retrieval.

The new radar datasets with single Doppler and triple Doppler analyses not only provide unique insights into the details of the ERC process and hurricane intensity change, but also allow for comparison of the wind retrieval between the ground-based radar and the P3 tail radar. The comparison points out that each platform has its own advantages and disadvantages. The P3 tail radar observations have higher spatial but lower temporal resolution, while the ground-based radar has higher temporal but lower spatial resolution when the radar is distant from the storm. This study has shown that the axisymmetric structure retrieved from these two platforms is in good agreement, suggesting confidence in the retrieval of TC circulations from single Doppler radar observations. On the other hand, the Fourier decomposition of asymmetric kinematic and convective structure from airborne pseudo-dual Doppler analysis could be potentially inconsistent with the single Doppler retrieval due to the spatial and temporal aliasing on the pseudo-dual Doppler analysis. It was found the reduced amplitude and phase shift during the flight leg of wavenumber 1 tangential wind was caused by the propagation of wavenumber 2 tangential wind. The pseudo-dual Doppler analysis is shown to have substantial impact on low-wavenumber structure unless the temporal evolution within one flight leg is considered. Future work with the time-dependent analysis of asymmetric structure to resolve the reflectivity and wind field is required.

REFERENCES


Bell, M. M., W.-C. Lee, C. A. Wolff, and H. Cai, 2013: A Solo-based automated quality control algorithm for airborne tail Doppler radar data. *J. Appl. Meteor. Climatol.*, **52 (11)**, 2509–2528, doi: 10.1175/JAMC-D-12-0283.1.

Bell, M. M. and M. T. Montgomery, 2008: Observed structure, evolution, and potential intensity of Category 5 Hurricane Isabel (2003) from 12 to 14 September. *Mon. Wea. Rev.*, **136 (6)**, 2023–2046, doi: 10.1175/2007MWR1858.1.

Bell, M. M., M. T. Montgomery, and W.-C. Lee, 2012: An axisymmetric view of concentric eyewall evolution in Hurricane Rita (2005). *J. Atmos. Sci.*, **69 (8)**, 2414–2432, doi: 10.1175/JAS-D-11-0167.1.

Black, M., J. Gamache, F. Marks, C. Samsury, and H. Willoughby, 2002: Eastern Pacific Hurricanes Jimena of 1991 and Olivia of 1994: The effect of vertical shear on structure and intensity. *Mon. Wea. Rev.*, **130 (9)**, 2291–2312, doi: 10.1175/1520-0493(2002)130<2291:EPHJOA>2.0.CO;2.

Black, M. L. and H. E. Willoughby, 1992: The Concentric Eyewall Cycle of Hurricane Gilbert. *Mon. Wea. Rev.*, **120**, 947–957, doi: 10.1175/1520-0493(1992)120<0947:TCECOH>2.0.CO;2.

Chan, J. C., 1984: An observational study of the physical processes responsible for tropical cyclone motion. *J. Atmos. Sci.*, **41 (6)**, 1036–1048, doi: 10.1175/1520-0469(1984)041<1036:AOSOTP>2.0.CO;2.

Chan, J. C. and W. M. Gray, 1982: Tropical cyclone movement and surrounding flow relationships. *Mon. Wea. Rev.*, **110 (10)**, 1354–1374, doi: 10.1175/1520-0493(1982)110<1354:TCMASF>2.0.CO;2.

Corbosiero, K. L. and J. Molinari, 2002: The effects of vertical wind shear on the distribution of convection in tropical cyclones. *Mon. Wea. Rev.*, **130 (8)**, 2110–2123, doi: 10.1175/1520-0493(2002)130<2110:TEOVWS>2.0.CO;2.

Corbosiero, K. L. and J. Molinari, 2003: The relationship between storm motion, vertical wind shear, and convective asymmetries in tropical cyclones. *J. Atmos. Sci.*, **60 (2)**, 366–376, doi: 10.1175/1520-0469(2003)060<0366:TRBSMV>2.0.CO;2.

Corbosiero, K. L., J. Molinari, A. R. Aiyyer, and M. L. Black, 2006: The structure and evolution of Hurricane Elena (1985). Part II: Convective asymmetries and evidence for vortex Rossby waves. *Mon. Wea. Rev.*, **134 (11)**, 3073–3091, doi: 10.1175/MWR3250.1.

DeMaria, M., M. Mainelli, L. K. Shay, J. A. Knaff, and J. Kaplan, 2005: Further improvements to the statistical hurricane intensity prediction scheme (SHIPS). *Wea. Forecasting*, **20 (4)**, 531–543, doi: 10.1175/WAF862.1.

Didlake, A. C., G. M. Heymsfield, P. D. Reasor, and S. R. Guimond, 2017: Concentric eyewall asymmetries in Hurricane Gonzalo (2014) observed by airborne radar. *Mon. Wea. Rev.*, **145**, 729–749, doi: 10.1175/MWR-D-16-0175.1.

Didlake, A. C. and R. A. Houze, 2011: Kinematics of the secondary eyewall observed in Hurricane Rita (2005). *J. Atmos. Sci.*, **68 (8)**, 1620–1636, doi: 10.1175/2011JAS3715.1.

Enagonio, J. and M. T. Montgomery, 2001: Tropical cyclogenesis via convectively forced vortex Rossby waves in a shallow water primitive equation model. *J. Atmos. Sci.*, **58 (7)**, 685–706, doi: 10.1175/1520-0469(2001)058<0685:TCVCFV>2.0.CO;2.

Griffin, J. S., R. W. Burpee, F. D. Marks, and J. L. Franklin, 1992: Real-time airborne analysis of aircraft data supporting operational hurricane forecasting. *Wea. Forecasting*, **7 (3)**, 480–490, doi: 10.1175/1520-0434(1992)007<0480:RTAAOA>2.0.CO;2.

Hence, D. A. and R. A. Houze, 2012: Vertical structure of tropical cyclones with concentric eyewalls as seen by the TRMM precipitation radar. *J. Atmos. Sci.*, **69 (3)**, 1021–1036, doi: 10.1175/JAS-D-11-0119.1.

Hoose, H. M. and J. A. Colón, 1970: Some aspects of the radar structure of Hurricane Beulah on September 9, 1967. *Mon. Wea. Rev.*, **98**, 529–533.

Houze, R. A., S. S. Chen, B. F. Smull, W.-C. Lee, and M. M. Bell, 2007: Hurricane intensity and eyewall replacement. *Science*, **315 (5816)**, 1235–1239, doi: 10.1126/science.1135650.

Jones, S. C., 1995: The evolution of vortices in vertical shear. I: Initially barotropic vortices. *Quart. J. Roy. Meteor. Soc.*, **121 (524)**, 821–851, doi: https://doi.org/10.1002/qj.49712152406.

Jou, B. J.-D., S.-M. Deng, and B. Chang, 1996: Determination of typhoon center and radius of maximum wind by using Doppler radar. *Atmos. Sci*, **24**, 1–24.

Jou, B. J.-D., W.-C. Lee, S.-P. Liu, and Y.-C. Kao, 2008: Generalized VTD retrieval of atmospheric vortex kinematic structure. Part I: Formulation and error analysis. *Mon. Wea. Rev.*, **136 (3)**, 995–1012, doi: 10.1175/2007MWR2116.1.

Kossin, J. P. and M. D. Eastin, 2001: Two distinct regimes in the kinematic and thermodynamic structure of the hurricane eye and eyewall. *J. Atmos. Sci.*, **58 (9)**, 1079–1090, doi: 10.1175/1520-0469(2001)058<1079:TDRITK>2.0.CO;2.

Kuo, H.-C., R. Williams, and J.-H. Chen, 1999: A possible mechanism for the eye rotation of Typhoon Herb. *J. Atmos. Sci.*, **56 (11)**, 1659–1673, doi: 10.1175/1520-0469(1999)056<1659:APMFTE>2.0.CO;2.

Lamb, H., 1932: *Hydrodynamics*. Cambridge university press.

Lee, W.-C. and M. M. Bell, 2007: Rapid intensification, eyewall contraction, and breakdown of Hurricane Charley (2004) near landfall. *Geophys. Res. Lett.*, **34 (2)**, doi: 10.1029/2006GL027889.

Lee, W.-C., B. J.-D. Jou, P.-L. Chang, and S.-M. Deng, 1999: Tropical cyclone kinematic structure retrieved from single-Doppler radar observations. Part I: Interpretation of Doppler velocity patterns and the GBVTD technique. *Mon. Wea. Rev.*, **127 (10)**, 2419–2439, doi: 10.1175/1520-0493(1999)127<2419:TCKSRF>2.0.CO;2.

Lee, W.-C., B. J.-D. Jou, P.-L. Chang, and F. D. Marks, 2000: Tropical cyclone kinematic structure retrieved from single-Doppler radar observations. Part III: Evolution and structures of Typhoon Alex (1987). *Mon. Wea. Rev.*, **128 (12)**, 3982–4001, doi: 10.1175/1520-0493(2000)129<3982:TCKSRF>2.0.CO;2.

Lee, W.-C. and F. D. Marks, 2000: Tropical cyclone kinematic structure retrieved from single-Doppler radar observations. Part II: The GBVTD-simplex center finding algorithm. *Mon. Wea. Rev.*, **128 (6)**, 1925–1936, doi: 10.1175/1520-0493(2000)128<1925:TCKSRF>2.0.CO;2.

Lee, W.-C., F. D. Marks, and R. E. Carbone, 1994: Velocity track display– A technique to extract real-time tropical cyclone circulations using a single airborne Doppler radar. *J. Atmos. Oceanic Technol.*, **11 (2)**, 337–356, doi: 10.1175/1520-0426(1994)011<0337:VTDTTE>2.0.CO;2.

Lorsolo, S. and A. Aksoy, 2012: Wavenumber analysis of azimuthally distributed data: Assessing maximum allowable gap size. *Mon. Wea. Rev.*, **140 (6)**, 1945–1956, doi: 10.1175/MWR-D-11-00219.1.

Marks, F. D., R. A. Houze, and J. F. Gamache, 1992: Dual-aircraft investigation of the inner core of Hurricane Norbert. Part I: Kinematic structure. *J. Atmos. Sci.*, **49 (11)**, 919–942, doi: 10.1175/1520-0469(1992)049<0919:DAIOTI>2.0.CO;2.

Montgomery, M. T. and R. J. Kallenbach, 1997: A theory for vortex rossby-waves and its application to spiral bands and intensity changes in hurricanes. *Quart. J. Roy. Meteor. Soc.*, **123 (538)**, 435–465, doi: https://doi.org/10.1002/qj.49712353810.

Moon, Y. and D. S. Nolan, 2015: Spiral rainbands in a numerical simulation of Hurricane Bill (2009). Part II: Propagation of inner rainbands. *J. Atmos. Sci.*, **72 (1)**, 191–215, doi: 10.1175/JAS-D-14-0056.1.

Reasor, P. D. and M. D. Eastin, 2012: Rapidly intensifying Hurricane Guillermo (1997). Part II: Resilience in shear. *Mon. Wea. Rev.*, **140 (2)**, 425–444, doi: 10.1175/MWR-D-11-00080.1.

Reasor, P. D., M. D. Eastin, and J. F. Gamache, 2009: Rapidly intensifying Hurricane Guillermo (1997). Part I: Low-wavenumber structure and evolution. *Mon. Wea. Rev.*, **137 (2)**, 603–631, doi: 10.1175/2008MWR2487.1.

Reasor, P. D. and M. T. Montgomery, 2001: Three-dimensional alignment and corotation of weak, TC-like vortices via linear vortex Rossby waves. *J. Atmos. Sci.*, **58 (16)**, 2306–2330, doi: 10.1175/1520-0469(2001)058<2306:TDAACO>2.0.CO;2.

Reasor, P. D., M. T. Montgomery, and L. D. Grasso, 2004: A new look at the problem of tropical cyclones in vertical shear flow: Vortex resiliency. *J. Atmos. Sci.*, **61 (1)**, 3–22, doi: 10.1175/1520-0469(2004)061<0003:ANLATP>2.0.CO;2.

Reasor, P. D., M. T. Montgomery, F. D. Marks, and J. F. Gamache, 2000: Low-wavenumber structure and evolution of the hurricane inner core observed by airborne dual-Doppler radar. *Mon. Wea. Rev.*, **128 (6)**, 1653–1680, doi: 10.1175/1520-0493(2000)128<1653:LWSAEO>2.0.CO;2.

Reasor, P. D., R. Rogers, and S. Lorsolo, 2013: Environmental flow impacts on tropical cyclone structure diagnosed from airborne Doppler radar composites. *Mon. Wea. Rev.*, **141 (9)**, 2949–2969, doi: 10.1175/MWR-D-12-00334.1.

Rios-Berrios, R. and R. D. Torn, 2017: Climatological analysis of tropical cyclone intensity changes under moderate vertical wind shear. *Mon. Wea. Rev.*, **145 (5)**, 1717–1738, doi: 10.1175/MWR-D-16-0350.1.

Rozoff, C. M., W. H. Schubert, and J. P. Kossin, 2008: Some dynamical aspects of tropical cyclone concentric eyewalls. *Quart. J. Roy. Meteor. Soc.*, **134 (632)**, 583–593, doi: https://doi.org/10.1002/qj.237.

Schubert, W. H., M. T. Montgomery, R. K. Taft, T. A. Guinn, S. R. Fulton, J. P. Kossin, and J. P. Edwards, 1999: Polygonal eyewalls, asymmetric eye contraction, and potential vorticity mixing in hurricanes. *J. Atmos. Sci.*, **56 (9)**, 1197–1223, doi: 10.1175/1520-0469(1999)056<1197:PEAECA>2.0.CO;2.

Sitkowski, M., J. P. Kossin, and C. M. Rozoff, 2011: Intensity and structure changes during hurricane eyewall replacement cycles. *Mon. Wea. Rev.*, **139 (12)**, 3829–3847.

Sitkowski, M., J. P. Kossin, C. M. Rozoff, and J. A. Knaff, 2012: Hurricane eyewall replacement cycle thermodynamics and the relict inner eyewall circulation. *Mon. Wea. Rev.*, **140 (12)**, 4035–4045, doi: 10.1175/MWR-D-11-00349.1.

Smith, R. K., M. T. Montgomery, and V. S. Nguyen, 2009: Tropical cyclone spin-up revisited. *Quart. J. Roy. Meteor. Soc.*, **135**, 1321–1335, doi: 10.1002/qj.428.

Tang, B. and K. Emanuel, 2012: A ventilation index for tropical cyclones. *Bull. Amer. Meteor. Soc.*, **93 (12)**, 1901–1912, doi: 10.1175/BAMS-D-11-00165.1.

Testud, J., P. H. Hildebrand, and W.-C. Lee, 1995: A procedure to correct airborne Doppler radar data for navigation errors using the echo returned from the earth's surface. *J. Atmos. Oceanic Technol.*, **12 (4)**, 800–820, doi: 10.1175/1520-0426(1995)012<0800:APTCAD>2.0.CO;2.

Uhlhorn, E. W., P. G. Black, J. L. Franklin, M. Goodberlet, J. Carswell, and A. S. Goldstein, 2007: Hurricane surface wind measurements from an operational stepped frequency microwave radiometer. *Mon. Wea. Rev.*, **135 (9)**, 3070–3085, doi: 10.1175/MWR3454.1.

Wang, Y., 2002: Vortex Rossby waves in a numerically simulated tropical cyclone. Part II: The role in tropical cyclone structure and intensity changes. *J. Atmos. Sci.*, **59 (7)**, 1239–1262, doi: 10.1175/1520-0469(2002)059<1239:VRWIAN>2.0.CO;2.

Wang, Y. and G. J. Holland, 1996: Tropical cyclone motion and evolution in vertical shear. *J. Atmos. Sci.*, **53 (22)**, 3313–3332, doi: 10.1175/1520-0469(1996)053<3313:TCMAEI>2.0.CO;2.

Willoughby, H. E.Clos, Shoreibah, and M. G., 1982: Concentric eye walls, secondary wind maxima, and the evolution of the hurricane vortex. *J. Atmos. Sci.*, **39**, 395–411, doi: 10.1175/1520-0469(1982)039<0395:CEWSWM>2.0.CO;2.

Willoughby, H. E. and M. B. Chelmow, 1982: Objective determination of hurricane tracks from aircraft observations. *Mon. Wea. Rev.*, **110 (9)**, 1298–1305, doi: 10.1175/1520-0493(1982)110<1298:ODOHTF>2.0.CO;2.

Wood, V. T. and R. A. Brown, 1992: Effects of radar proximity on single-Doppler velocity signatures of axisymmetric rotation and divergence. *Mon. Wea. Rev.*, **120 (12)**, 2798–2807, doi: 10.1175/1520-0493(1992)120<2798:EORPOS>2.0.CO;2.

Zhao, K., W.-C. Lee, and B. J.-D. Jou, 2008: Single doppler radar observation of the concentric eyewall in Typhoon Saomai, 2006, near landfall. *Geophys. Res. Lett.*, **35 (7)**, doi: 10.1029/2007GL032773.